Naval Research Laboratory

Washington, DC 20375-5320

NRL/MR/7322--20-10,176

VTR for Implementation of Wave-Ocean Coupling in COAMPS in both the Near-shore and Offshore Ocean

Paul J. Martin

Kacey L. Edwards

Jayaram Veeramony

Cheryl Ann Blain

Timothy J. Campbell

Ocean Dynamics and Prediction Branch
Ocean Sciences Division

October 7, 2020

REPORT DOCUMENTATION PAGE

Form Approved
OMB No. 0704-0188

1. REPORT DATE *(DD-MM-YYYY)*	**2. REPORT TYPE**	**3. DATES COVERED** *(From - To)*
07-10-2020	NRL Memorandum Report	10-01-2017 – 9-30-2019

4. TITLE AND SUBTITLE

VTR for Implementation of Wave-Ocean Coupling in COAMPS in both the Nearshore and Offshore Ocean

5a. CONTRACT NUMBER

5b. GRANT NUMBER
N0001420WX00896

5c. PROGRAM ELEMENT NUMBER
0603207N

6. AUTHOR(S)

Paul Martin, Jay Veeramony, Kacey Edwards, Cheryl Ann Blain, and Tim Campbell

5d. PROJECT NUMBER
FY17-PRO-06

5e. TASK NUMBER

5f. WORK UNIT NUMBER
5097

7. PERFORMING ORGANIZATION NAME(S) AND ADDRESS(ES)

Naval Research Laboratory
4555 Overlook Avenue, SW
Washington, DC 20375-5320

8. PERFORMING ORGANIZATION REPORT NUMBER

NRL/MR/7322--20-10,176

9. SPONSORING / MONITORING AGENCY NAME(S) AND ADDRESS(ES)

Office of Naval Research
One Liberty Center
875 N. Randolph Street, Suite 1425
Arlington, VA 22203-1995

10. SPONSOR / MONITOR'S ACRONYM(S)

ONR

11. SPONSOR / MONITOR'S REPORT NUMBER(S)

12. DISTRIBUTION / AVAILABILITY STATEMENT

DISTRIBUTION STATEMENT A: Approved for public release; distribution is unlimited.

13. SUPPLEMENTARY NOTES

14. ABSTRACT

Ocean-wave coupling within the Coupled Ocean Atmospheric Modeling System (COAMPS) is adapted to capture wave-driven circulation and mixing in shallow, nearshore environments including the surf zone. Enhancements to the ocean model, NCOM, include a depth dependent wave radiation stress, enhanced surface roughness, and an increased turbulent kinetic energy to account for mixing due to wave breaking. The wave roller energy is captured through the addition of a parametric roller model which introduces a lag in wave momentum transport due to wave breaking. Lastly, wave dissipation forcing is demonstrated as an alternative to wave radiation stress gradient forcing. Thorough testing and evaluation using idealized and field test cases demonstrate that the new wave forcing in NCOM produces a vertical distribution of surf zone currents and mixing that are consistent with observations. Addition of the wave roller further improves realism of the surf zone currents, in magnitude and spatial distribution, for simple bathymetry configurations. Unfortunately for non-linear bathyemtry profiles, such as barred beaches, the results are less satisfactory with discontinuities in surf zone currents likely to occur. Wave dissipation forcing for the test cases examined is essentially interchangeable with wave radiation stress gradient forcing with respect to significant wave height, salinity and temperature profiles, and water levels.

15. SUBJECT TERMS

Ocean-Wave Coupling
Nearshore
Surfzone
3D Wave Radiation Stress
Wave Dissipation
Roller Model

16. SECURITY CLASSIFICATION OF:			**17. LIMITATION OF ABSTRACT**	**18. NUMBER OF PAGES**	**19a. NAME OF RESPONSIBLE PERSON**
a. REPORT	**b. ABSTRACT**	**c. THIS PAGE**			Cheryl Ann Blain, Ph.D.
Unclassified Unlimited	Unclassified Unlimited	Unclassified Unlimited	Unclassified Unlimited	67	**19b. TELEPHONE NUMBER** *(include area code)* (228) 688-5450

Standard Form 298 (Rev. 8-98)
Prescribed by ANSI Std. Z39.18

This page intentionally left blank.

CONTENTS

FIGURES

TABLES

This page intentionally left blank.

EXECUTIVE SUMMARY

Coupled ocean-wave interactions play an important role in circulation and transport over the range of scales spanning from the continental shelf to nearshore regimes. The prediction of these dynamics is addressed by the Coupled Ocean Atmospheric Modeling System (COAMPS), a modeling suite of atmospheric, ocean circulation, and wave models (Allard et al., 2014; Campbell et al., 2010). For the ocean-wave coupling described herein, the Navy Coastal Ocean Model (NCOM) (Martin et al., 1998; Barron et al. 2006) is the ocean circulation model and Simulating Waves Nearshore (SWAN) is the wave model (Booij et al., 1996). Existing mechanisms implemented within NCOM for capturing wave effects within the ocean model are designed for regional (kilometer scale) dynamics. For high-resolution (10's of meters) applications near the coast, additional wave-ocean interactions must be accounted for. To that end, the following enhancements are incorporated into NCOM: a depth-dependent (three-dimensional) wave radiation stress (WRS), and the addition of increased surface roughness and surface turbulent kinetic energy (TKE) to account for enhanced mixing from breaking waves in the surf zone. The addition of a "roller model" accounts for the effect of wave rollers in the surf zone, which delays the transfer of momentum from the waves to the ocean currents and thereby affects the location and strength of currents generated by breaking waves. Lastly, surface wave dissipation forcing is developed as an alternative to the application of wave radiation stress gradients. Each of the enhancements listed has undergone testing and evaluation using idealized test cases having expected solutions and field cases with available observations.

The three-dimensional WRS implemented in NCOM is of the functional form discussed by Mellor (2003, 2005, 2013, 2015). Several alternatives for vertical dependence of the WRS (especially the highly uncertain 3rd term) are explored including an empirical relation proposed by Kumar et al (2011), and various functions of the type $\cosh^2$, $\sinh^2$, and cosh sinh. The empirical findings of Kumar et al. (2012) are used to enhance surface roughness (i.e., half the height of the dominant breaking waves) and TKE (i.e., 5% of the total wave dissipation) in the surf zone. Details of all ocean-wave coupling terms, their definition, implementation, and usage in NCOM are provided. Testing each of these nearshore wave physics enhancements in NCOM is completed using the idealized case of an along shore uniform beach with a uniform bottom slope forced with waves propagating onshore at an angle with respect to the shoreline. Results produce a total current in the surf zone that is weak with onshore flow at the surface and offshore flow at the bottom, consistent with observations. The maximum rate of mixing within the surf zone shifts from the center of the water column to near or at the surface which is expected from strong surface wave breaking. The enhanced mixing due to breaking waves does not affect the Stokes current, but reduces the vertical shear of the total currents within the surf zone. Outside the surf zone, vertical mixing and currents remain unchanged.

The turbulent area that forms on the face of a wave at the point of breaking is represented in COAMPS by the parametric definition of wave roller energy by Reniers and Battjes (1997) using

the form for wave roller area published by Warner et al. (2008). The parametric wave roller energy modifies the surface momentum balance of the waves as captured by the radiation stress gradients. Test cases to evaluate performance of the roller model include an idealized plane beach bathymetric surface, two parameterized barred bathymetric surfaces, and the barred beach field test site at Duck, North Carolina. The latter test case is part of the validation test suite for the current operational nearshore system.

Over three different bathymetric surfaces, the idealized test cases demonstrate that the roller approximation is capable of producing the desired effect of creating a lag in wave momentum transport that occurs due to wave breaking. The wave roller approximation moves the peak along shore current shoreward, increasing the current magnitude and broadening the current peak. When a bar is present in the bathymetric surface, an unrealistic discontinuity forms in the current field. Analyses show the cause is zero valued wave forces at the maxima of the radiation stresses, producing a discontinuity in the resulting currents. The field test cases, which also include bathymetric bars, similarly result in velocity discontinuities.

As long as the waves are resolved with sufficiently high grid resolution and there is no wave generation within the domain, wave radiation stress gradients perform well as the primary mechanism by which wave momentum is applied to hydrodynamic models in order to drive wave-induced circulation. However, if either of these conditions is not met, the momentum transferred from the waves to the ocean will typically be in error. We implement an alternative approach, wave dissipation forcing using the formulation of Tang et al. (2004), to transfer momentum from waves to the ocean.

Evaluation of the two forms of wave momentum flux transfer, the radiation stress gradient based formulation (WRSG) and the dissipation based formulation (WD), are compared in simulations over two test cases, a large-scale regional domain (US East), (approximately 4km resolution), and a high resolution (approximately 400m), smaller coastal domain (Chesapekae Bay). The coupled ocean-wave system using each formulation, WRSG and WD, in run for the entire year of 2015. Model-data comparisons for significant wave heights, salinity and temperature profiles, and water levels spanned the entire year as well as shorter 10-15 day periods for three specific case studies (January 2015 North American Blizzard, Hurricane Joaquin, September 2015, and Hurricane Kate, November 2015). Overall, the wave dissipation based method (WD) was more stable, and performed slightly better than the wave radiation stress gradient (WRSG) approach for temperature and salinity profiles. However, differences between the two methods of wave momentum transfer are essentially negligible for the various test cases studied, with no appreciable differences in significant wave height or water level.

VTR FOR IMPLEMENTATION OF WAVE-OCEAN COUPLING IN COAMPS IN BOTH THE NEARSHORE AND OFFSHORE OCEAN

1. INTRODUCTION

Coupled ocean-wave interactions play an important role in circulation and transport over the range of scales spanning from the continental shelf to nearshore regimes. The prediction of these dynamics is addressed by the Coupled Ocean Atmospheric Modeling System (COAMPS). COAMPS is a modeling suite of atmospheric, ocean circulation, and wave models that share information using the Earth System Modeling Framework (ESMF) (Allard et al., 2014; Campbell et al., 2010). For ocean-wave coupling addressed in this manuscript, the Navy Coastal Ocean Model (NCOM) is the ocean circulation model. The bases of NCOM are the Princeton Ocean Model (POM) (Blumberg and Mellor, 1983, 1987) and the Sigma/Z-level Model (SZM) (Martin et al., 1998; Barron et al. 2006). NCOM is a free-surface model derived from the primitive equations with the hydrostatic, Boussinesq, and incompressible approximations. One of the wave models within COAMPS and considered here is the Simulating Waves Nearshore (SWAN) model (Booij et al., 1996). SWAN is a phase-averaged wave model that solves the action density equation in discrete form. SWAN includes physically- and observation-based parameterizations for the wind input (Donelan et al., 2005; Donelan et al., 2006; Babanin and Young, 2005; Tsagareli et al., 2010; Rogers et al., 2012) and dissipation terms (Banner et al., 2000; Babanin and Young, 2005; Young and Babanin, 2006; Babanin et al., 2010).

Prior to the work described herein, ocean-wave coupling within NCOM was designed for medium- and coarse-resolution offshore and coastal applications. The mechanisms implemented for capturing wave effects within the ocean model were limited to the two vector components of the wave-radiation stress gradient (WRSG), two vector components of the Stokes drift current (SDC) from the waves, and the amplitude, frequency, and direction of the wave orbital motion near the ocean bottom (e.g., Allard et al. 2012).

For high-resolution (10's of meters) applications near the coast, additional wave-ocean interactions must be accounted for. To that end, the following enhancements are incorporated into NCOM: a depth-dependent (three-dimensional) wave radiation stress (WRS), as well as the addition of increased surface roughness and increased surface turbulent kinetic energy (TKE) from breaking waves in the surf zone (SFZ) to increase vertical mixing in the SFZ. Furthermore, the addition of a so-called "roller model" accounts for the effect of wave rollers in the SFZ, which delays the transfer of momentum from the waves to the ocean currents and thereby affects the location and strength of the currents generated by the breaking waves. The final modifications involve implementation of a surface wave dissipation forcing as an alternative to the application of wave radiation stress gradients. All of the new wave forcing implementations presented are tested and evaluated using a variety of idealized and realistic applications whose results are included and discussed herein.

Manuscript approved October 7, 2020.

2. WAVE FORCING IN NCOM

The surface gravity wave forcing currently utilized in NCOM (e.g. Allard et al. 2014) is decribed first. The Stokes current is used in NCOM to augment advection of the NCOM fields, to account for surface wave effects on vertical mixing, e.g., mixing due to Langmuir circulations (Martin et al., 2013), and to provide a Stokes-Coriolis forcing term in the momentum equations. The amplitude, frequency, and direction of the wave orbital motion near the bottom are used to compute the enhanced bottom drag due to the wave-bottom boundary layer (Grant and Madsen, 1982; Soulsby, 1995; Mellor, 2002). The WRSG accounts for the transfer of momentum from the waves to the ocean currents (Longuet-Higgins and Stewart, 1964).

The momentum transfer from breaking waves to ocean currents is of crucial importance in the surfzone (SFZ), since it is the main driver of both the longshore (LS) and cross-shore (CS) currents in this area. In the nearshore, applying the 2D WRSG just at the surface results in a current that is too surface intensive, especially in the wave shoaling zone (SHZ) just outside the SFZ, where the WRSG is directed offshore due to the increasing height of the waves as they encounter a shallowing bottom. Hence, it was decided to implement a three-dimensional (3D) wave radiation stress (WRS), i.e., with a depth-dependence, to see if that would provide more realistic currents both in the SFZ and the SHZ. Papers discussing the derivation and use of a 3D WRS to force ocean currents in the nearshore are rare and are mainly comprised of the papers by Mellor (2003, 2005, 2008, 2011, 2013, 2015, 2016). In addition to the depth-dependent WRS, both increased surface roughness and increased surface turbulent kinetic energy (TKE) from breaking waves in the SFZ are considered to increase vertical mixing in the SFZ.

2.1 Implementation of New Wave Forcing Physics in NCOM

2.1.1 Implementation of 3D WRS

There has not been a lot of work published on the depth-dependence of the WRS forcing of the ocean currents by the waves. Our implemtation of a 3D WRSG in NCOM was guided primarily by the papers of Mellor (2003, 2005, 2013, 2015). An important aspect of the 3D WRSG is that its vertical integral should give the same value as the 2D WRSG computed from the waves that we have previously used in NCOM.

The form for the depth-dependent WRS from Mellor (2003, 2005, 2013, 2015) is given by

$$S_{ab} = kE\left(\frac{k_a k_b}{k^2} F_{cc} F_{cs} - \delta_{ab} F_{sc} F_{ss} + \delta_{ab}(F_{cc} F_{cs} + F_{sc} F_{ss} - F_{cs} F_{ss})\right), \tag{1}$$

where S_{ab} is the WRS, a and b refer to the x or y coordinate, k is the wave number, E is the wave energy, and δ is the Kronica delta, which is 1 if $a = b$ and zero otherwise. F here is a dimensionless function of depth, where the first subscript, c or s, represents a numerator of $\cosh(k(D+z))$ or $\sinh(k(D+z))$, respectively, the second subscript, c or s, represents a denominator of $\cosh(kD)$ or $\sinh(kD)$, respectively, D is the total water depth, and z is the distance below the surface, positive upwards, i.e., $z < 0$.

The implementation of the 3D WRSG within NCOM's horizontal momentum equations is given by

$$\frac{\partial u}{\partial t} = ... - \frac{\partial S_{xb}}{\partial b} = ... - \frac{\partial S_{xx}}{\partial x} - \frac{\partial S_{xy}}{\partial y}, \tag{2}$$

$$\frac{\partial v}{\partial t} = ... - \frac{\partial S_{yb}}{\partial b} = ... - \frac{\partial S_{yx}}{\partial x} - \frac{\partial S_{yy}}{\partial y}, \tag{3}$$

where u and v are the two horizontal components of the momentum and t is the time. In sigma coordinates this becomes

$$\frac{\partial(\Delta z u)}{\partial t} = ... - \frac{\partial(\Delta z S_{xx})}{\partial x} - \frac{\partial(\Delta z S_{xy})}{\partial y}, \tag{4}$$

$$\frac{\partial(\Delta z v)}{\partial t} = ... - \frac{\partial(\Delta z S_{yx})}{\partial x} - \frac{\partial(\Delta z S_{yy})}{\partial y}, \tag{5}$$

where Δz is the layer thickness. The procedure used to calculate the 3D WRSG ensures that the vertical integral of the 3D WRSG is the same as the 2D WRSG previously used, and is the same as the horizontal gradient of the 2D WRS calculated from the vertical integral of the 3D WRS that will be input to NCOM.

2.1.2 Implementation of surface roughness and TKE flux from breaking waves

The surface TKE flux and surface roughness due to breaking waves, which are inputs to the turbulent mixing models used in NCOM to compute vertical mixing, were previously parameterized just in terms of the local surface wind stress. The surface TKE flux can be estimated from the wind stress as (Craig and Banner, 1994)

$$K_q \frac{\partial q^2}{\partial z} = 2\alpha u_*^3, \tag{6}$$

where K_q is the vertical diffusivity for the TKE, q^2 is twice the TKE, α is a constant with a value of 100, and u_* is the surface friction velocity. The surface roughness can be estimated from the wind stress using the Charnock (1955) formula as (Craig and Banner, 1994)

$$s_r = c_{harnok} u_*^2 / g \tag{7}$$

where s_r is the surface roughness, c_{harnok} is a constant with a current default value of 2000, and g is the gravitational constant.

These parameterizations are clearly inadequate in the coastal ocean where waves are breaking due to the shallowing bottom and not necessarily due to the local wind forcing. Even in the open ocean, a parameterization of the surface TKE flux and roughness based on the current local wind stress does not account for the effects of fetch and the history of the winds and the wave propagation

on the local wave field. When using wave forcing from a wave model, one can use the wave model's estimate of the current, local, wave conditions to estimate the values of the surface TKE flux and roughness due to the waves.

Within the surf zone, Kumar et al. (2012) suggested (a) parameterizing the surface TKE flux due to the breaking waves as some fraction of the total wave dissipation, and (b) parameterizing the surface roughness due to the breakng waves as some fraction of the significant height of the breaking waves. Kumar et al. found that using a large fraction of the wave dissipation for the surface TKE flux resulted in mixing that was too strong, and settled on using a fraction of 5%. For the surface roughness, they used half the significant height of the breaking waves. The values of the surface TKE flux and the surface roughness currently used in NCOM are the maximum of (i) the input value from the wave model computed as in Kumar et al. (2012), i.e. 5% of the total wave dissipation and half the significant height of breaking waves, and (ii) the value estimated from the local wind stress, as noted above in Eq. (6) and (7).

2.2 Summary of All NCOM Wave Forcing Inputs

The 3D WRSG is computed within NCOM instead of being passed in because the calculation of the 3D WRSG depends on specific conditions within the ocean model that are not accurately known a'priori.

The depths of the input wave forcing are defined in their own input file ozwav_*nn*.D, where *nn* is the nest/grid number. This is an ascii (plain text) file containing the number of depths l_{wav} on the first line of the file, followed by l_{wav} depths, each depth on its own line. The input wave forcing depths z_{wav} start at zero and decrease downward (i.e., $z_{wav} <= 0$) using a stretched grid (to provide increased resolution near the surface) and ending with $z_{wav}(l_{wav})$, which is typically a value like -300.0 m, i.e., a depth where the surface wave forcing is negligibly small.

For the input WRS fields, in order to increase the resolution of the input fields in shallow water, the input depths z_{wav} are treated like a sigma coordinate grid when the total water depth d is less than $-z_{wav}(l_{wav})$, i.e., for $d <= -z_{wav}(l_{wav})$ the depths of the input WRS fields are computed as $z = -d\, z_{wav}(k)/z_{wav}(l_{wav})$. For $d >= -z_{wav}(l_{wav})$, the input depths are just defined as $z = z_{wav}$. There is an option to treat the depths for the input SDC fields the same way (i.e., by setting the input parameter flag for the SDC as indsdc=2).

The wave forcing fields themselves are all input within a single, binary, direct-access file owave_*nn*.A. An associated ascii file owave_*nn*.B is used to define the date and time values for the input wave-forcing fields, along with an integer flag for each set of fields denoting if that set of fields is provided within the wave-forcing input file. Note that a particular wave-forcing field that is requested for an NCOM run, but is not provided, will trigger a fatal error.

The wave forcing fields currently implemented in NCOM are listed in Table 1, along with some additional information about each field, including its dimensions (the fields are either 3D, i.e., depth-dependent, or 2D), and its associated input flag.

The input SDC consists of two depth-dependent fields, u_s and v_s, that are horizontally located at the corresponding staggered u and v velocity locations, and are vertically located at the depths

Table 1—List of wave forcing fields in NCOM

Wave Forcing Field	Units	Dimensions	Input Flag
SDC x-component	m/s	n x m x l_{wav}	indsdc
SDC y-component	m/s	n x m x l_{wav}	indsdc
Wave current amplitude near bottom	m/s	n x m	indwbc
Wave current frequency near bottom	Hz	n x m	indwbc
Wave current direction near bottom	$^\circ$	n x m	indwbc
S_{xx} (WRS)	m^2/s^2	n x m x l_{wav}	indrsg
S_{xy} (WRS)	m^2/s^2	n x m x l_{wav}	indrsg
S_{yy} (WRS)	m^2/s^2	n x m x l_{wav}	indrsg
Energy dissipation from breaking waves	m^2/s^3	n x m	indwdis
Wave-induced surface roughness	m	n x m	indwruf
Wave orbital turbulence production	m^2/s^3	n x m x l_{wav}	indwtp

$z = z_{wav}$ if indsdc=1, or at the depths $z = -d\, z_{wav}(k)/z_{wav}(l_{wav})$ if both indsdc=2 and $d < -z_{wav}(l_{wav})$ as discussed above. Within NCOM, the SDC is vertically interpolated from its input depths to the mid-layer depths of the NCOM vertical grid.

The wave-bottom-current amplitude, frequency, and direction are used to enhance the bottom drag in shallow water when there is a wave-bottom boundary layer near the sea bed (Mellor 2002). The near-bottom velocity from the wave motion increases the total near-bottom velocity and therefore increases the bottom drag. The enhancement of the bottom drag in shallow water due to the surface waves is parameterized in NCOM using the method of Soulsby (1995).

The input WRS consists of three depth-dependent fields, S_{xx}, S_{xy}, and S_{yy}, which are the x, x-y cross, and y terms of the input WRS tensor, respectively. These fields are located horizontally at the grid-cell centers, and vertically at the depths $z = -d\, z_{wav}(k)/z_{wav}(l_{wav})$ if $d < -z_{wav}(l_{wav})$ and at depths $z = z_{wav}$ if $d >= -z_{wav}(l_{wav})$ as discussed above.. The WRSG is computed from the WRS within NCOM.

The energy dissipation from breaking waves is used to provide a surface TKE flux from the breaking waves. Kumar et al. (2012) suggest using a value for the surface TKE flux of 5% of the total dissipation from the waves, and this is the value input to NCOM, i.e., 5% of the dissipation from the wave model from wave breaking and whitecapping.

The wave-induced surface roughness is used to parameterize the surface roughness due to breaking waves. Kumar et al. (2012) suggest using a value for the wave-induced surface roughness of half the significant wave height in areas where significant wave breaking is occurring, and this is the value input to NCOM.

NCOM previously estimated the surface TKE flux and surface roughness from the input wind stress; however, this is inadequate to account for the surface TKE flux and roughness when the waves are breaking due to shallowing water, rather than to the wind forcing. Hence, the values of

surface TKE flux and roughness currently used are the maximum of the input value from the wave model and the value estimated from the wind stress (Eq. (6) and (7)) as just described previously and computed by Kumar et al. (2012).

The wave orbital turbulence production is a parameterization of turbulence production caused by non-breaking surface waves by Babanin (2006) and Babanin and Haus (2009). The input to NCOM is a turbulence production profile computed from the local wave spectrum, which is added to the vertical shear and buoyancy production terms of the TKE equations of the vertical mixing scheme used in NCOM.

2.3 Testing of New Wave Forcing Physics in Surfzone

The implementation of the 3D WRSG in NCOM was tested using the simple, idealized case of a LS-uniform beach with a uniform bottom slope of 1/80, and with a JONSWAP spectrum of waves propagating onshore at an angle of 10° with repect to the shoreline. This has been a commonly-used case for testing wave-ocean coupling in the nearshore (e.g., Haas and Warner, 2009; Uchiyama et al., 2010; Kumar et al., 2011; Kumar et al., 2012). Note that it is the angle of the incoming waves with respect to the shoreline that generates the LS current, which is driven by the component of the WRSG in the LS direction. The strength of this LS current is primarily determined by the balance between the LS component of the WRSG and the bottom drag.

Figure 1 shows LS and CS profiles of the Stokes current from the incoming waves from SWAN, the NCOM ocean current driven by the WRSG from SWAN with vertical dependence given by Eq. (1), and the combined current consisting of the Stokes current plus NCOM's WRSG-driven current. The Stokes current has only a weak vertical dependence in shallow water. However, the NCOM WRSG-driven CS current is strongly offshore at the surface in the SFZ, and this carries over to the total, combined CS current which, in the SFZ, is offshore at the surface and onshore near the bottom. (Note that the total CS current must satisfy continuity, i.e., once a steady solution is reached, the offshore and onshore components of the CS current must balance so that there is no net CS flow.) This is the opposite of the onshore at the surface, offshore near the bottom, overturning circulation expected of the CS current in the SFZ (e.g., Kumar et al. 2011). Hence, the Mellor formula Eq. (1) for the vertical dependence of the WRSG does not seem to be consistent with the expected profile of the total current within the SFZ.

We could not find much else in the literature regarding the depth-dependence of the WRS. This led us to try some alternative formulations for the vertical dependence of the WRS, specifically for the 3rd (last) term in Eq. (1), which seemed to be the most uncertain part of Mellor's WRS based on the variations of the presentation of this term within the full series of papers on the 3D WRS that he published.

Kumar et al. (2011) used an empirical formula

$$F^*(z) = \cosh\left(\frac{2\pi(D+z)}{H_{rms}}\right) \tag{8}$$

to reduce the surface-intensiveness of the 2D WRSG, where H_{rms} is the RMS wave height. With a scaling factor to provide the correct vertical integral, this becomes

$$F(z) = \frac{\pi}{kH_{rms}} \cosh(\frac{2\pi(D+z)}{H_{rms}}) \tag{9}$$

Figure 2 shows LS and CS profiles of the Stokes, NCOM, and total current using Kumar et al.'s depth-dependence Eq. (9) for the 3rd term in Eq. (1). Within the SFZ the total current is onshore at the surface and offshore near the bottom, which is consistent with observations. Within the SHZ; however, there is a fairly strong (about 20 cm/s) offshore current near the surface and a slightly weaker onshore current near the bottom. Since there is not much observational support for a such a relatively strong offshore surface current in the SHZ, it was decided to try some alternative, depth-dependent functions.

We tried a number of different depth-dependent functions for the 3rd term of Eq. (1) of the type used by Mellor. These included functions of the type $\cosh^2$, $\sinh^2$, and cosh sinh. Figure 3 shows LS and CS profiles of the Stokes, NCOM, and total current using the depth-dependent function

$$F(z) = (\cosh^2(k(D+z))/(\cos(kD)\sinh(kD)+kD) + FcsFss)/2, \tag{10}$$

which is an equal weighting of functions $\cosh^2$ and cosh sinh, along with normalization factors to give the correct vertical integral. This gives a total current in the SFZ that is onshore at the surface and offshore at the bottom, consistent with observations. Within the SHZ the current is weak, which is at least not inconsistent with observations. Hence, Eq. (10) is the form of the depth-dependent WRS currently implemented in NCOM.

All the NCOM results shown so far used NCOM's current vertical mixing with the Kantha and Clayson (2004) mixing model, but do not include the enhanced surface roughness and surface TKE input from breaking waves that one would expect to contribute to vertical mixing within the SFZ. As a result, the turbulent length scale, the TKE, and the rate of turbulent mixing within the SFZ are relatively small near the surface, and the maximums occur near the middle of the water column (Fig. 4a). The KC04 mixing scheme includes the shear production of TKE from the square of the vertical shear of the NCOM Eulerian (model) current, and also from the product of the vertical shears of the NCOM Eulerian current and the Stokes current. Hence, there is some vertical mixing occurring in both the SFZ and SHZ just due to the waves, i.e., without accounting for any wind mixing.

Kumar et al. (2012) suggest using a surface roughness within the SFZ of half the height of the dominant breaking waves (i.e., half the RMS wave height), and a surface TKE flux of 5% of the total wave dissipation to increase the vertical mixing near the surface within the SFZ caused by the breaking waves. Figure 4 illustrates the difference in the rate of vertical mixing resulting from this change. The maximum rate of mixing within the SFZ shifts from near the center of the water column (Fig. 4a) to near or at the surface (Fig. 4b), which is more what one would expect from strong surface wave breaking. Outside the SFZ the vertical mixing is unchanged.

Figure 5 shows the effect of this change in the vertical mixing on the LS and CS currents. One can compare Fig. 5 with Fig. 3, where enhanced mixing due to breaking waves is not fully accounted

for. The increased mixing does not affect the Stokes current, but reduces the vertical shear of the NCOM and total currents within the SFZ. Outside the SFZ the currents are not much changed.

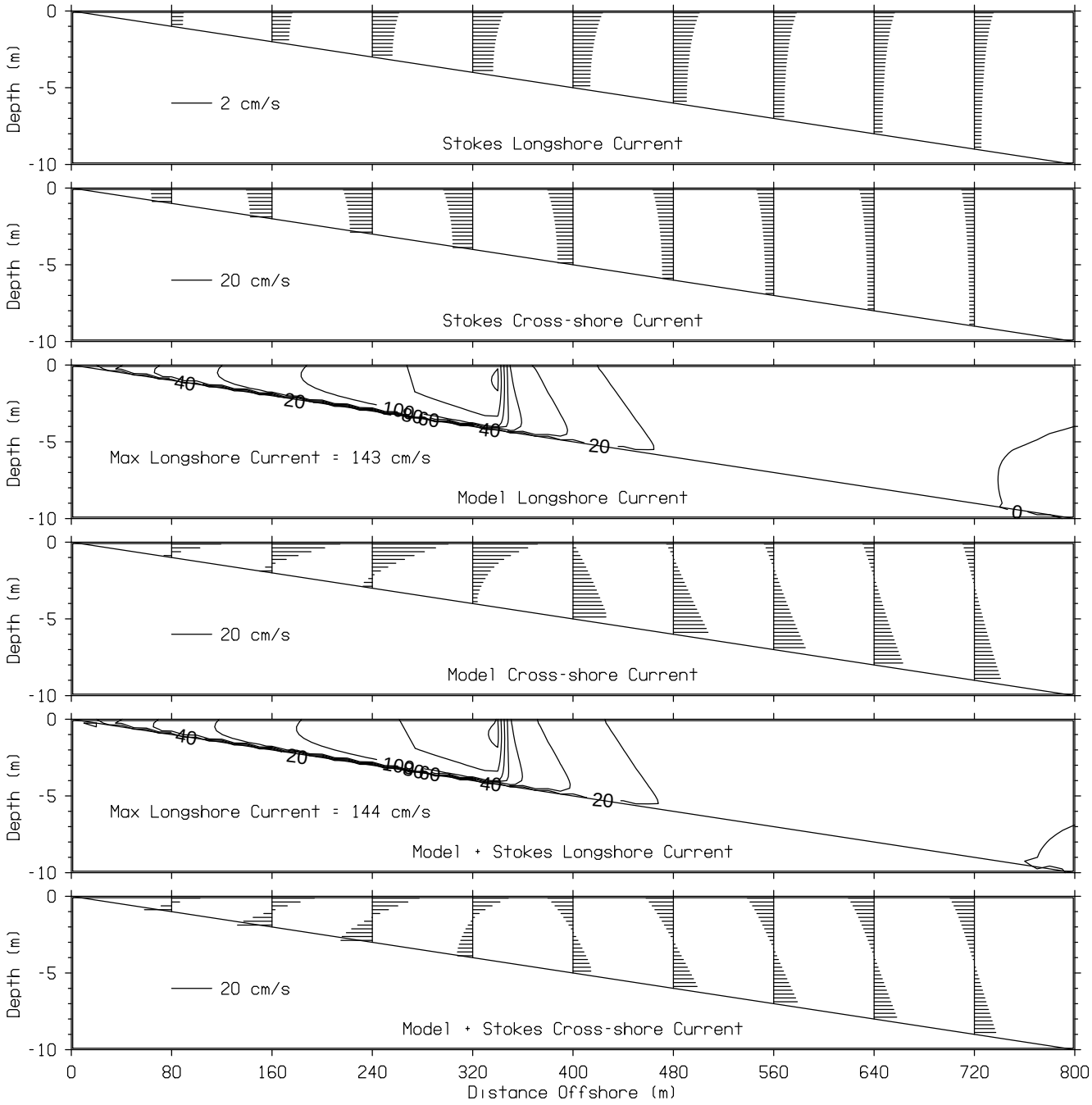

Fig. 1—LS and CS components of the Stokes current, the NCOM (model) current, and the total (NCOM + Stokes) current for the Mellor WRS.

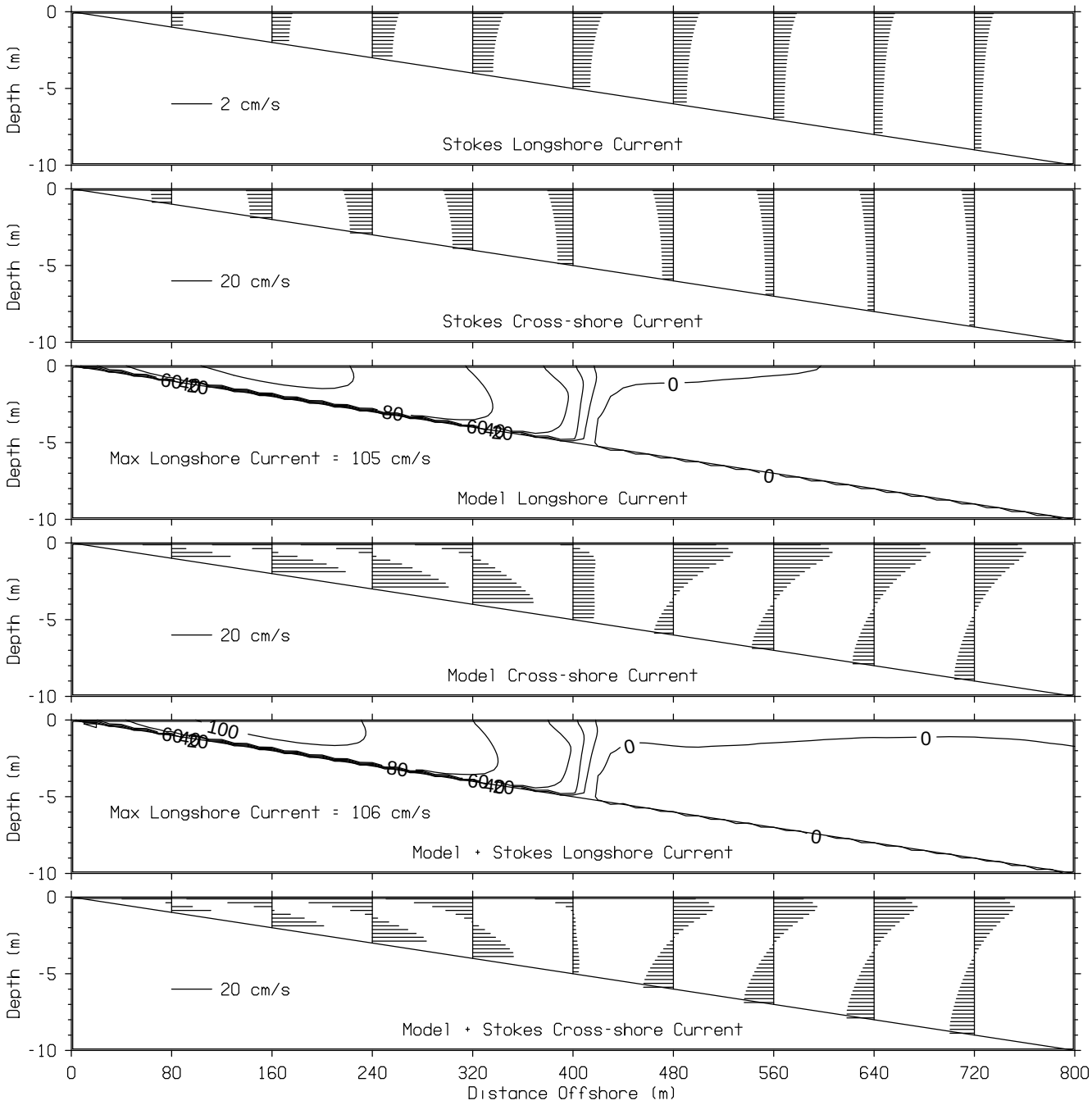

Fig. 2—LS and CS components of the Stokes current, the NCOM (model) current, and the total (NCOM + Stokes) current for the Mellor WRS with its 3rd term replaced with a cosh function scaled by the RMS wave height.

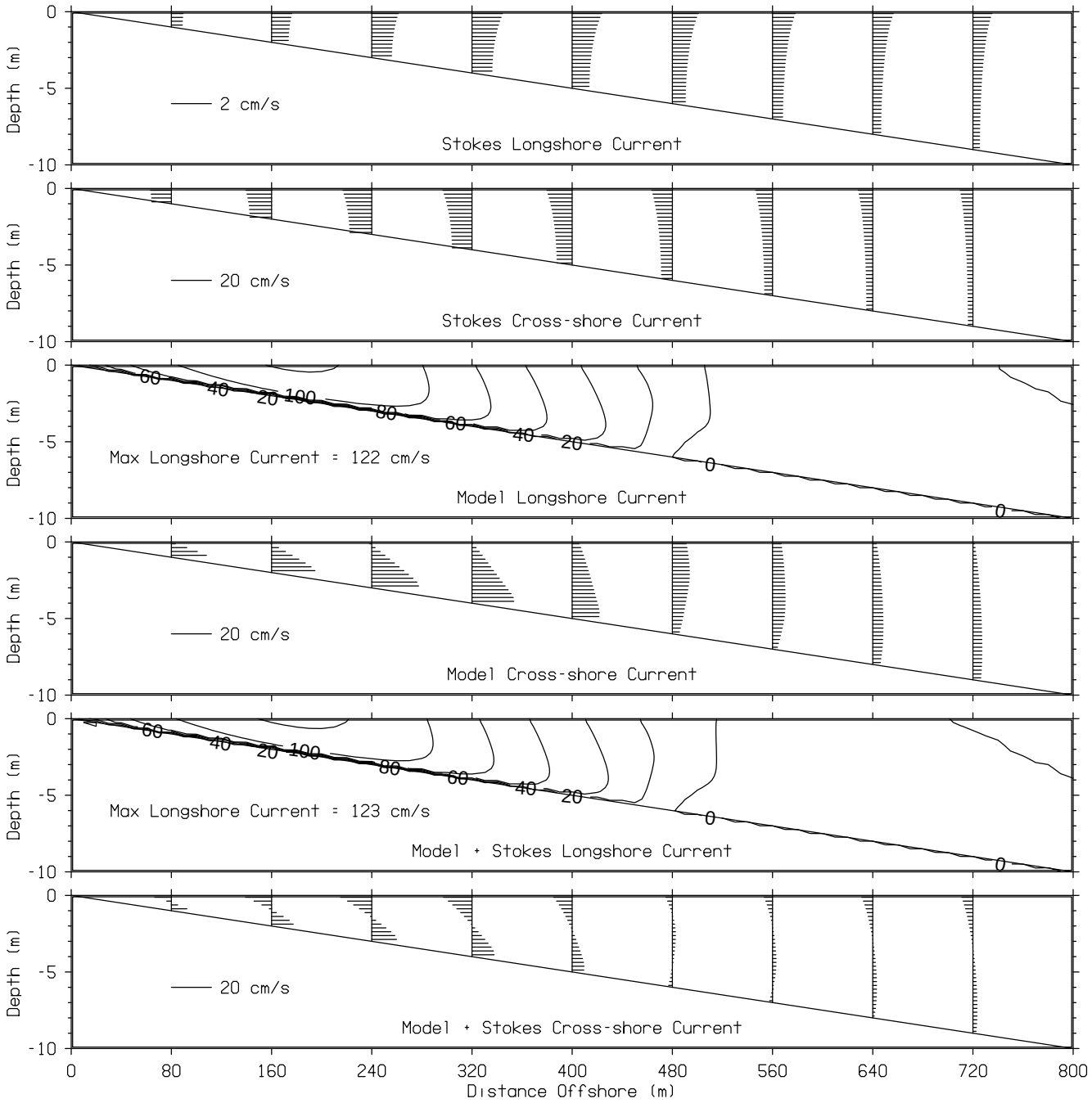

Fig. 3—LS and CS components of the Stokes current, the NCOM (model) current, and the total (NCOM + Stokes) current for the Mellor WRS with its 3rd term replaced with an equal weighting of $\cosh^2$ and cosh sinh depth functions.

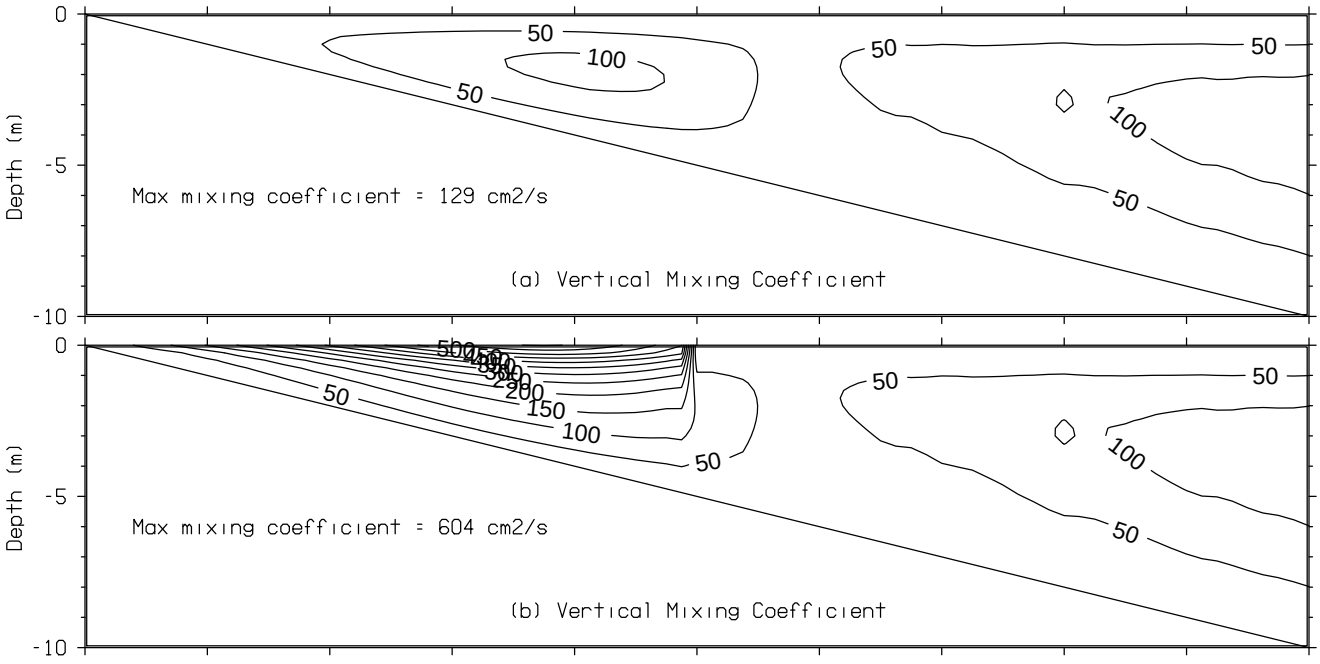

Fig. 4—Plots of vertical mixing coefficient for momentum for simulation without (a) and with (b) surface roughness and surface TKE input from breaking waves in the surfzone.

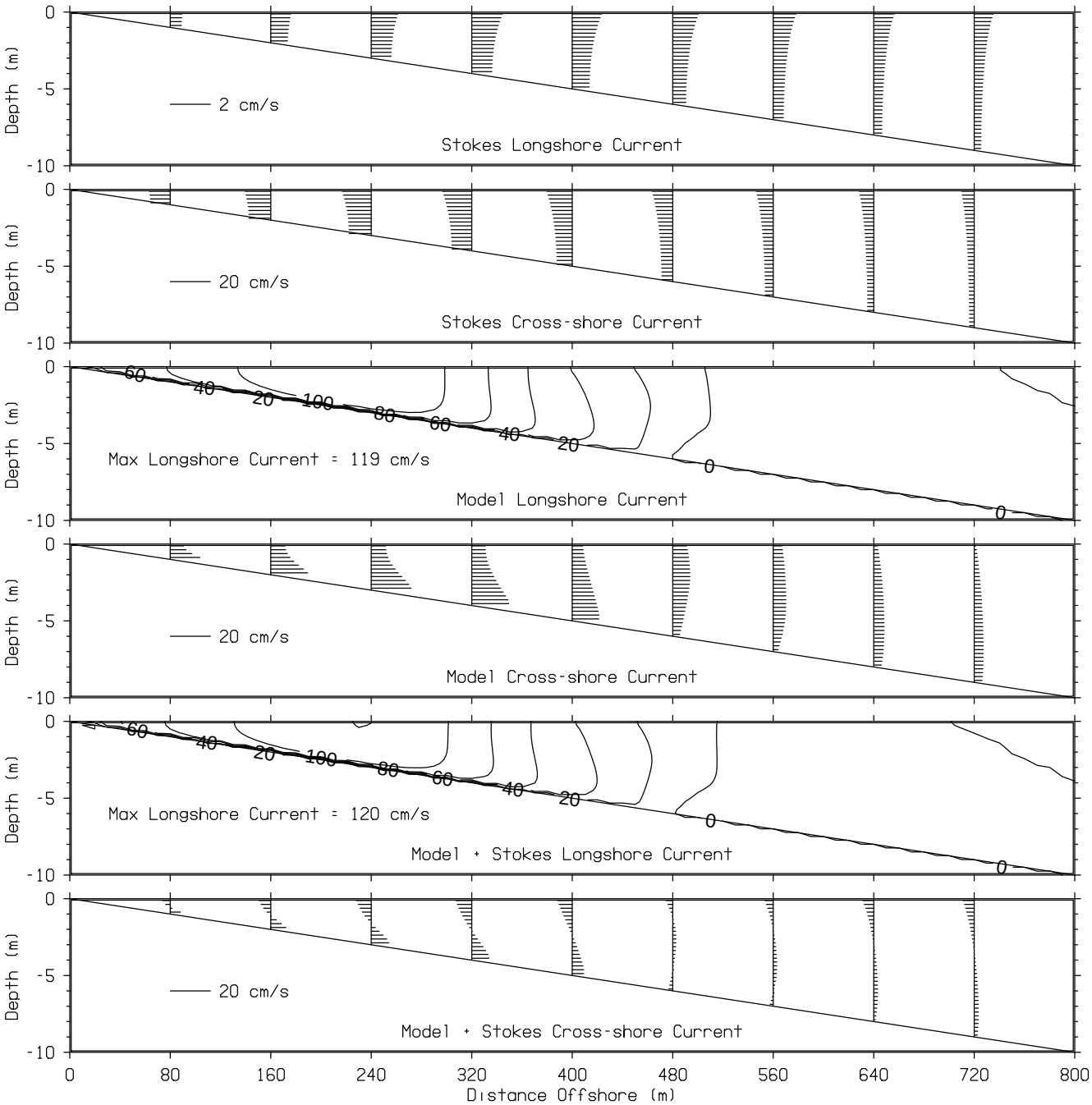

Fig. 5—LS and CS components of the Stokes current, the NCOM (model) current, and the total (NCOM + Stokes) current for the Mellor WRS with its 3rd term replaced with an equal weighting of $\cosh^2$ and cosh sinh depth functions and the addition of enhanced surface roughness and surface TKE flux from breaking waves.

3. WAVE ROLLER APPROXIMATION

As waves propagate from the inner shelf across the surf zone to the shoreline, they undergo a transformation. Near-sinusoidal, inner-shelf waves propagate towards the shore. As depth decreases, the waves begin to interact with the bathymetry and slow. The sinusoidal shape transforms to an asymmetric, pitched-forward shape. Eventually, the wave breaks in a dramatic loss of energy to the water column.

At the point of breaking, a turbulent area forms on the face of the wave (Sven, 1984a; Sven, 1984b, Lippmann et al., 1996). This area is called the wave roller. We focus on the effects of the turbulent roller on surf-zone currents over idealized planar and barred bathymetric profiles.

Wave transformation models typically begin with a wave energy balance equation and a momentum balance. The change in wave energy as it propagates along a bathymetric profile is balanced by the decay of organized wave energy (Lippmann et al., 1996), and it is assumed that organized wave energy is instantly converted to turbulent energy (Nairn et al., 1990). The wave energy balance assumes monochromatic waves, and bathymetric alongshore uniformity (Lippmann et al., 1996). Additionally, balance is maintained between the change in momentum, the elevation, and the bottom stress. The change in momentum is described as the gradient in radiation stress and is a driving force for currents.

The typical wave transformation models work well for linear waves. However, the turbulent roller part of a breaking wave adds nonlinearity to the problem (Apotsos et al., 1997). Nonetheless, the typical model works reasonably well on planar beaches and predicts wave heights and setup on barred beaches (Apotsos, 2007; Smith et al., 1993; Roelvink and Stive, 1989; Nairn et al., 1990; Reniers et al., 1995). The complication of a barred profile is realized in the calculation of the wave forcing (Lippmann et al., 1996). On barred beaches, typical wave transformation models routinely result in two maxima in forcing and, if mixing is omitted, two maxima in alongshore current velocity (Smith et al., 1993; Church and Thornton, 1993).

Because the largest gradients in the radiation stresses occur where wave energy dissipation is the greatest, the typical wave transformation model results in wave forcing that puts the maximum alongshore current at the bar crest and near the shore (Reniers and Battjes, 1997), where wave height decay is greatest (Smith et al., 1993). Additionally, in the bar trough, where waves reform, the wave forcing is zero, driving no currents in this location (Smith et al., 1993). However, data from many laboratory and field experiments show that the currents are strongest shoreward of the bar crest and often in the bar trough (Reniers and Battjes, 1997). Smith et al. (1993) report "an unexpected, persistent broad peak in the current velocity in the trough between the nearshore bar and the shore."

Several theories to explain the observed current distributions in the cross-shore direction exist. One explanation is related to the turbulent roller part of the breaking wave. It is suggested that the wave momentum transport occurs over a transition zone, rather than at the point of breaking, causing a lag in the transfer of momentum from the bar crest to a point shoreward of the bar crest (Lippmann et al., 1996; Nairn et al., 1990; Apotsos et al., 2007). The lag is thought to exist because of the time needed to convert organized kinetic and potential energy to small-scale, dissipative turbulent motion (Roelvink and Stive, 1989), and Roelink and Stive (1989) suggest

extending the horrizontal momentum balance to "account for the affects of the turbulent energy on the radiation stress magnitude."

Two techniques have been investigated for storing the wave momentum and transferring it over the transition zone. One is the inclusion of turbulent kinetic energy (TKE) and wave induced stress (Nairn et al., 1990; Roelvink and Stive, 1989; Smith et al., 1993; Church and Thornton, 1993). We will focus on the alternative, a parametric definition of the wave roller contribution to the momentum balance equation. In this approach, the wave roller serves as a storage or trap of kinetic energy, leading to the lag previously discribed (Nairn et al., 1990). In their investigation, Nairn et al. (1990) found that both approaches produced similar results, and that the influence of the transition zone had a considerable, positive effect on their predictions. Roelvink and Stive (1989) found that accounting for the lag significantly improved prediction of the position of the maximum gradients in undertow and the position of maximum undertow. In their field study at Duck, NC and in their model development and evaluation, Smith et al. (1993) show the shoreward shift of turbulent energy to be essential in producing the observed, persistent, high-magnitude current in the bar trough. Reniers and Battjes (1997) show that neglecting the wave roller in the alongshore momentum balance results in disagreement of the computed and observed maximum shear stress and in premature release of momentum resulting in an understimation of the alongshore current in the trough. Apotsos et al. (2007) found that wave-roller inclusion moved the transition from setdown to setup onshore by six meters on average. Ruessink et al. (2001), too, found that wave rollers were essential in predicting the position of maximum velocity in the cross shore and in increasing the velocity in the trough.

3.1 Description of Wave Roller Approximation

NCOM and SWAN are coupled using the balance between wave momentum (gradients in radiation stresses), elevation, and the bottom stress (Longuet-Higgins and Stewart, 1962, 1964; Apotsos et al., 2007). The roller energy is given by (Reniers and Battjes, 1997) as

$$E_r = \frac{\rho A c^2}{2L}, \tag{11}$$

where ρ is water density, c is wave speed, L is wave length, and A is the wave roller area given by Svendsen (1984a) in a form published by Warner et al. (2008),

$$A = \frac{\alpha}{\sqrt{2}} H_s L Q_b, \tag{12}$$

where Q_b is the percent wave breaking and α is the constant 0.06. H_s is the significant wave height defined as

$$H_s = 4\sqrt{m_0}, \tag{13}$$

where m_0 is the total wave energy. Therefore, the wave roller energy is given as

$$E_r = \frac{2\rho\alpha\sqrt{m_0} Q_b c^2}{\sqrt{2}}, \tag{14}$$

and the S_{xy} and S_{yy} radiation stress tensors are given as

$$S_{xy} = E_w \left\{ \frac{c_g}{c} sin(\bar{\theta}) cos(\bar{\theta}) \right\} + 2E_r [sin(\bar{\theta}) cos(\bar{\theta})] \tag{15}$$

$$S_{yy} = E_w \left\{ [sin^2(\bar{\theta}) + 1] \frac{c_g}{c} - \frac{1}{2} \right\} + 2E_r [sin^2(\bar{\theta})]. \tag{16}$$

3.2 Test Cases Used for Testing Wave Roller

Two cases are considered for testing and validating the wave roller approximation. The first tests are performed using idealized bathymetric profiles – one plane sloping and two barred scenarios. No data exist for the idealized case, so model-model comparisons provide a first-look at how the roller approximation affects the wave-forced currents. For validation, modeled circulation parameters are compared to in situ observations for the Duck94 field experiment conducted at the Field Research Facility at Duck, North Carolina. As with the idealized test case, we use model-model comparisons to observe the effects of the roller approximation on wave-forced currents. We compare the surface currents at the water surface because the wave forces that drive the currents are applied at the surface; therefore, we see the greatest effect of employing the roller approximation at the surface. The model-data comparisons tell us how well the model performs with and without the roller approximation. However, because the in situ measurements are taken at varying water column locations and not at the surface, these comparisons do not directly validate the roller approximation. The idealized and field test cases are described in the following subsections.

3.2.1 Idealized Test Cases

We evaluate the COAMPS system with the wave roller approximation over three idealized bathymetric surfaces. All model domains are resolved horizontally to 10 meters. Vertically, NCOM is resolved using 11 sigma-layers. We neglect wind in NCOM and SWAN, and at the NCOM offshore boundary, we neglect forcing. Periodic boundary conditions are prescribed on the lateral NCOM boundaries. JONSWAP spectra are prescribed at the open SWAN boundaries given a root mean square wave height (H_{rms}) of 2 meters, period (T) of 10 seconds, and direction (θ) of 10 nautical degrees.

The idealized bathymetric surfaces are uniform in the alongshore direction, and include a plane beach slope of 1:80, a shallow bar (Fig. 6, top), and a deep bar (Fig. 6, bottom). In the plane beach case, a transition from offshore to onshore flow in the surface layers occurs around 400 meters from the shore. The shallow bar is relatively close to shore, approximately 174 meters from the shore, and is shoreward of the transition seen in the plane beach case. The crest of the shallow bar is approximately 0.5 meters below the water surface. Here, the waves reform, but at heights of less than 0.5 meter, as shown in Fig. 7. The deep bar, however, is located near the transition seen in the plane beach case at a distance of approximately 361 meters from shore, and the depth of the bar crest is about 3 meters. As shown in Fig. 7, waves propagating along this profile reform shoreward of the bar before breaking again near the shore. We refer to these three bathymetric profiles as the Plane Beach (PB), Shallow Bar (SB), and Deep Bar (DB) Test Cases.

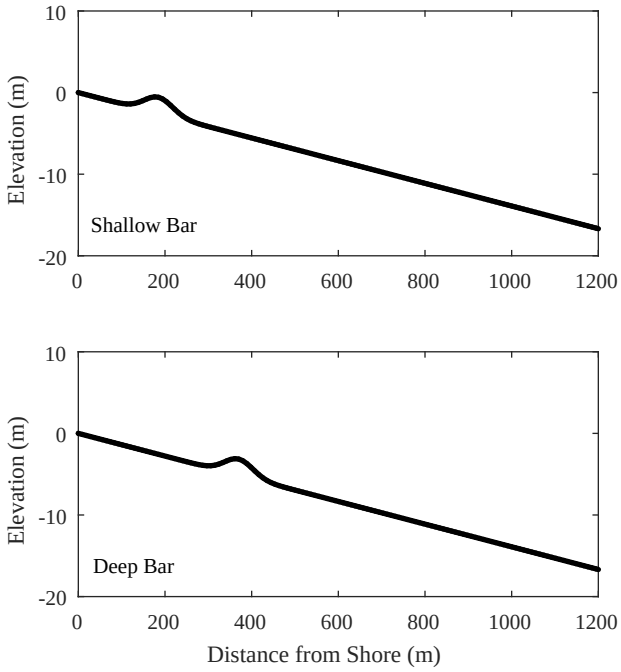

Fig. 6—Idealized bar profile of the shallow (top) bar and the deep (bottom) bar.

3.2.2 Field Test Case

We apply the COAMPS system with the wave roller approximation to the Field Research Facility in Duck, NC and model the conditions of the DUCK94 experiment (Birkemeier et al., 1996) mimicking testing performed by Hsu et al. (2006) and Hsu et al. (2008). All model domains are resolved horizontally to 10 meters in the across shore and 15 meters in the along shore directions. Vertically, NCOM is resolved using 21 sigma layers. Wind speeds and directions from the 8 meter gage array (Fig. 8, right; middle and bottom) are applied to the NCOM and SWAN models. At the NCOM offshore boundary, we neglect forcing, but the change in water depth caused by tides is accounted for by adding the tide derived from the mean water level at the 8 meter gage array (Fig. 8, right; top) to the water depths. JONSWAP spectra are prescribed at the open SWAN boundaries given the H_{rms}, T, and θ reported by the 8-meter gage array (Fig. 8, right; top, middle, and bottom, repectively). We evaluate the model for various offshore conditions at the 8-meter gage array during October 1994. Specifically, we look at October 10-12, October 19, and October 26, 1994.

The 10-12 October time period is characterized by significant wave heights of 0.5 to just over 2 meters, with an average of 1.82 meters for the three days. These waves have peak periods of 5-7 seconds and travel relatively obliquely from the south east. We expect waves at these angles to produce strong along shore flows. Along the cross shore gage array, the bathymetric profile features one bar positioned about 240 m from shore. There is some variation in the bathymetric profile between the three days of 10-12 October 1994; however, the position of the bar is fairly constant, and offshore of the bar the profiles do not vary. The largest variation in the three days is shoreward of the bar; on October 10 and 11 the trough is more filled and the shoreward face of the bar is

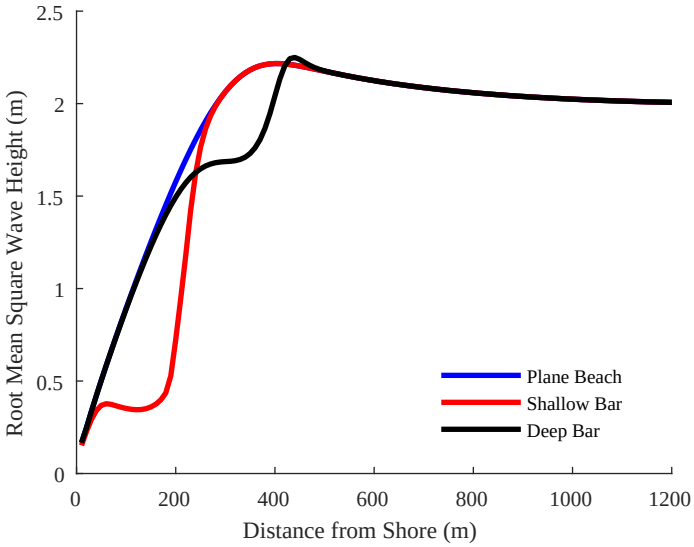

Fig. 7—Root mean square wave heights for the Plane Beach (blue), Shallow Bar (red), and Deep Bar (black) Test Cases.

gentler sloping. On October 12, the trough is more carved out, and the shoreward slope of the bar is steeper sloping (Fig. 9).

Mid-October, a storm produces significant wave heights up to 4 meters and drastically changes the bathymetric profile along the cross-shore instrument array. The profiles from October 19 and 26, 1994 are characterized by double bars. The largest of the bars is located approximately 330 meters from shore, and a smaller bar exists shoreward about 270 meters from shore (Fig. 9). Longer period waves of 12-15 seconds dominate October 19, 1994, and significant wave heights on this day average about 1.5 meters. On October 19, 1994, waves approach the beach from the north east at a smaller angle than we see earlier in the month. In fact, the waves are so close to shore normal that rip currents may be generated.

3.3 Model Configuration Used to Test Wave Roller

3.3.1 Idealized Test Cases

The model is configured with wave-to-ocean coupling; information is exchanged at a 1 minute interval. Both the wave and ocean grids are resolved to approximately 10 meters, with 64 grid points in the cross shore direction and 122 grid points in the along shore direction. The bathymetry is determined by repeating a cross shore profile in the along shore direction. The cross shore profiles are described in the Test Cases Section of this report. The ocean model is vertically resolved using 11 sigma layers, and it runs with a time step of 1 second. The wave model is run in stationary mode. The ocean and wave models utilize cyclic or repeating boundary conditions. Wind forcing is neglected. Using 24 processors, 6 hour hind casts completed in approximately 8 minutes, with and without the roller approximation.

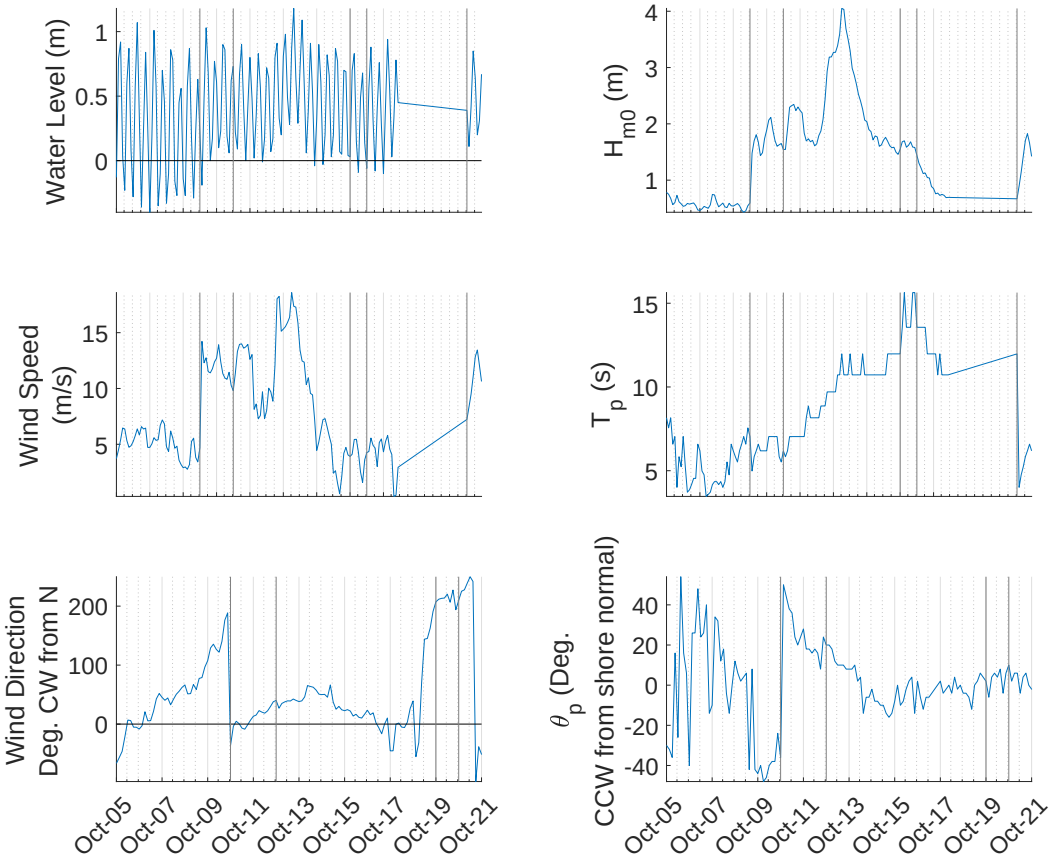

Fig. 8—In situ measurments taken at the 8 meter array and used as input to the model. Black vertical lines on each plot mark the times of model analyses and discussion. Parameters shown are water elevation (right, top), wind speed (right, middle), wind direction (right, bottom), significant waveheight (left, top), peak wave period (right, middle), and peak wave direction (right, bottom).

3.3.2 Field Test Case

The model is configured for the Duck94 experiment using only wave-to-ocean coupling; information is exchanged between the models every hour. Both the wave and ocean models are resolved to 15 meters in the along shore direction and 10 meters in the cross shore direction, with 85 grid points in the cross shore direction. The ocean model grid has 116 grid points in the along shore direction. The wave model grid is extended on the lateral boundaries to remove boundary effects from the area of study. As a result, the wave model has 216 grid points in the along shore direction. The bathymetry is prescribed using field surveys from the experiment, as previously described. The ocean model is vertically resolved using 21 sigma layers and runs with a time step of 20 milliseconds. The wave model is run in stationary mode. The ocean model utilizes cyclic boundary conditions in the along shore direction. Input and boundary conditions are prescribed using data collected at the experiment's 8 meter gage array. Wind measurements are applied as constant input to the wave and ocean models. The tide is used to adjust the bathymetric surface to account for changes

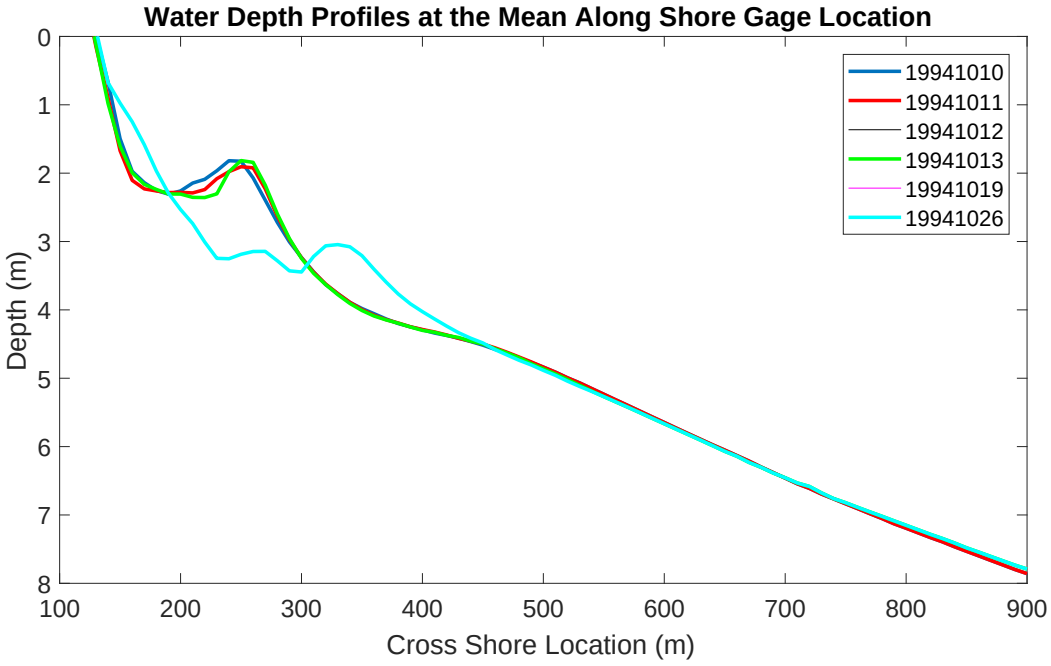

Fig. 9—Bathymetric profiles measured at the cross shore gage array. Profiles are shown for 1994 October 10 (blue), 11 (red), 12 (black), 13 (green), 19 (magenta), and 26 (cyan).

in tidal elevation. Measurements of significant wave height, wave period, and wave direction are applied at the wave lateral and offshore boundaries as parametric boundary conditions. Using 28 processors, 3 hour hind casts completed in approximately 1 hour, 16 seconds, with and without the roller approximation.

3.4 Results From Testing Wave Roller

3.4.1 Idealized Test Cases

For all three test cases, we omit results showing the effect of applying the wave roller approximation to the prediction of H_{rms} because, as were the findings of Lippmann et al. (1996), Roelvink and Stive (1989), and Smith et al. (1993), the wave roller does not effect the H_{rms} predictions. The greatest effects of applying the wave roller approximation are seen in the cross shore profiles of cross shore and alongshore velocities.

In results from the plane beach test case, as expected, we see a transition in the surface layers from offshore flow (red) to onshore flow (blue). The transition is located about 370 meters from shore. Shoreward of this surface transition, we see a return flow or undertow (red) down the bathymetric slope (Fig. 10, top). When the wave roller approximation is included, the transition moves shoreward approximately 40 meters (Fig. 10, middle). Additionally, we see that waves drive an along shore current and the peak of the surface along shore current moves shoreward when the wave roller approximation is added (Fig. 11, bottom). Although the peak along shore current is confined to the surface layers, we see a shoreward shift in along shore current between 300 and 400 meters from shore by visually comparing the top and middle panels of Fig. 11.

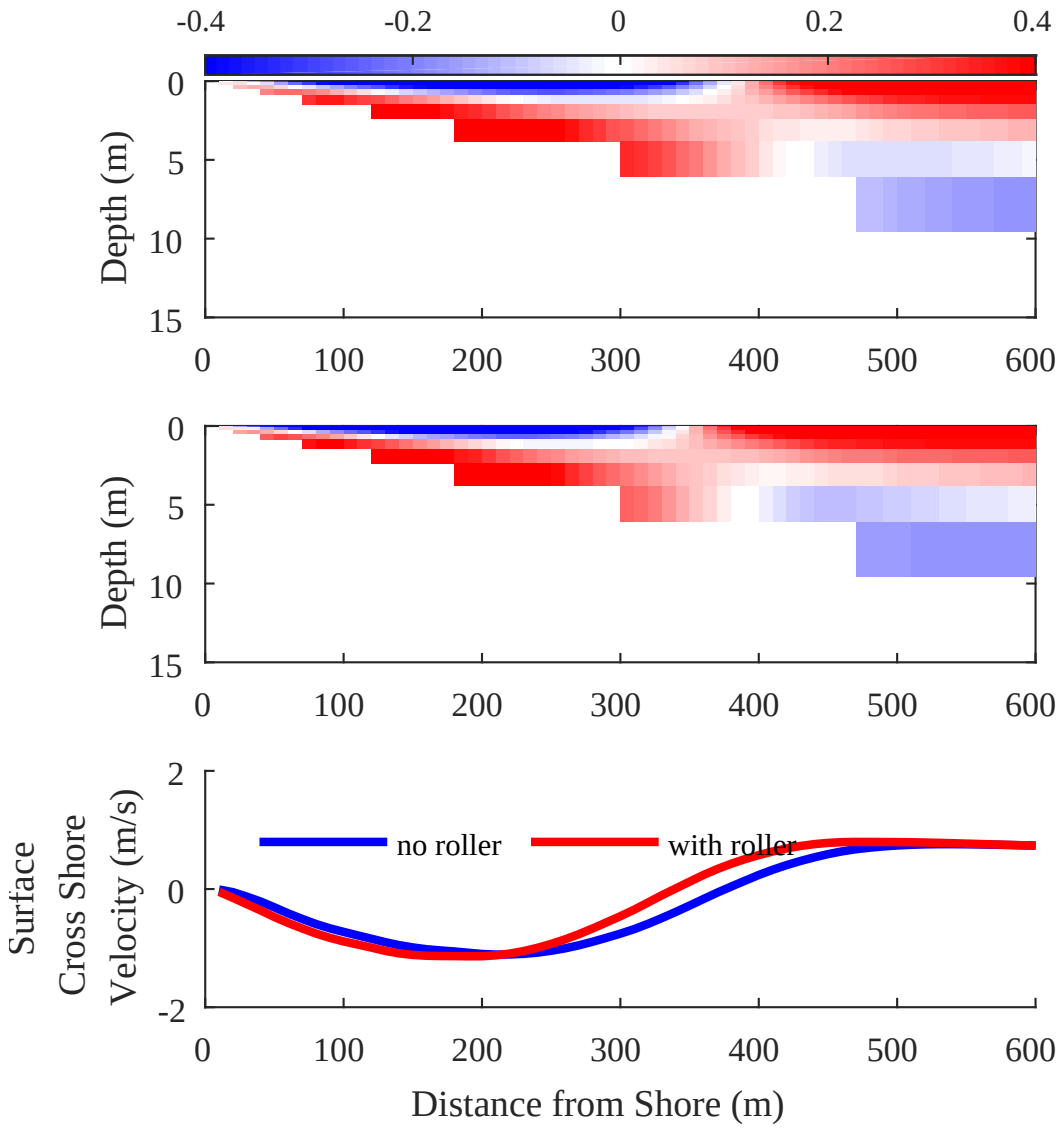

Fig. 10—Plane Beach Test Case cross shore current slices over depth without (top) and with (middle) the wave roller approximation, where red indicates offshore flow and blue indicates onshore flow, and a comparison of the surface cross shore current profile with and without the wave roller approximation (bottom).

Results from the Shallow Bar Test Case show in Fig. 12 (top) that the typical wave transformation model maintains the plane beach location of the transition from offshore (red) to onshore (blue) flow at the surface. Shoreward of this location, the surface flow is directed onshore with a return flow down the seaward slope of the bar. Additionally, around the same location, a wave driven alongshore flow begins to develop. The alongshore current is strongest on the seaward slope of the bar up to the crest with little alongshore flow on the shoreward slope of the bar (Fig. 13, top). When the wave roller approximation is included, the strongest alongshore currents are centered over the bar crest and down the shoreward slope into the trough (Fig. 13, middle), and the cross shore shoreward surface current and return flow persist closer to shore (Fig. 12, middle and

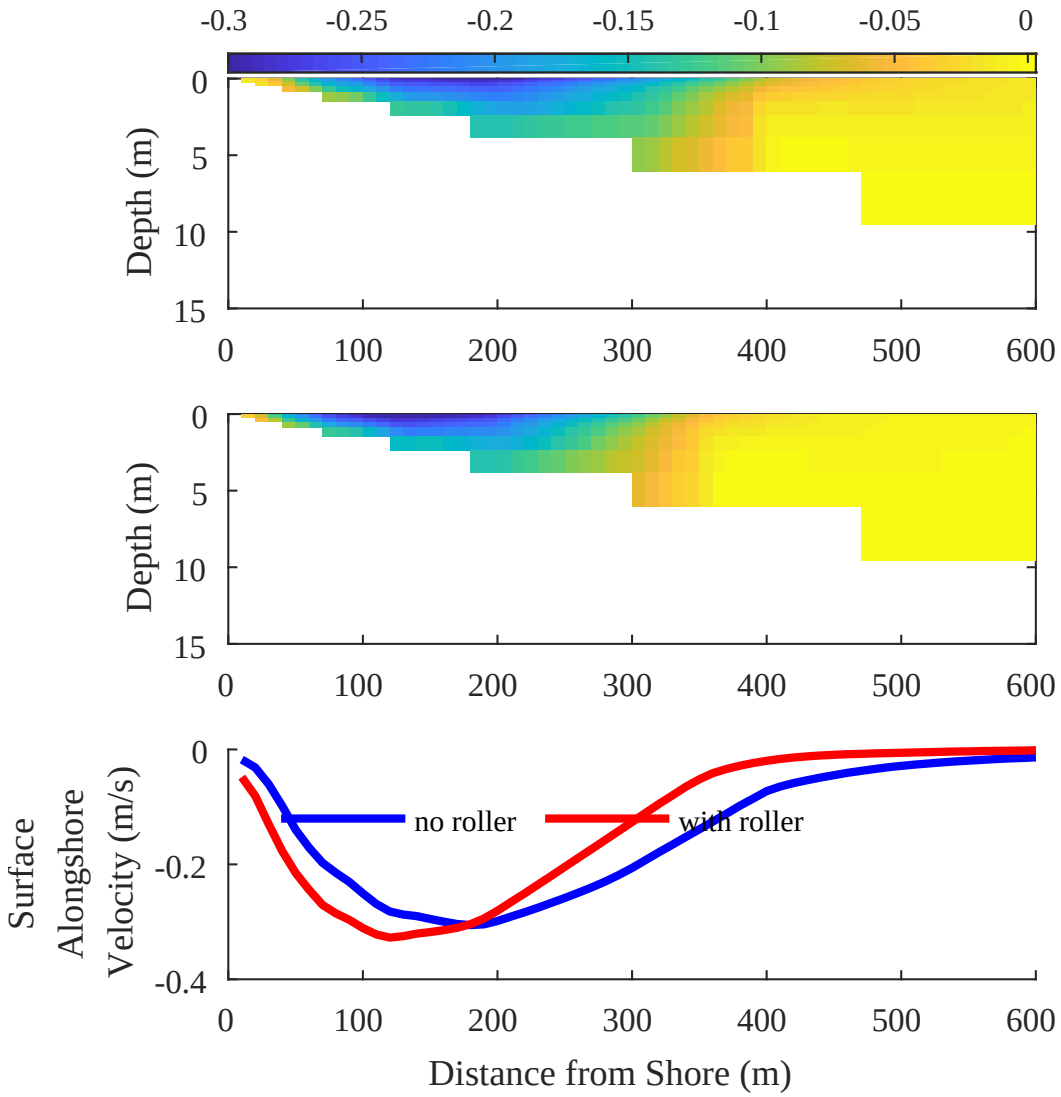

Fig. 11—Plane Beach Test Case alongshore current slices over depth without (top) and with (middle) the wave roller approximation, and a comparison of the surface alongshore current profile with and without the wave roller approximation (bottom)..

bottom). However, a discontinuity develops in both the alongshore (Fig. 13, middle) and cross shore (Fig. 12, middle) velocities between 250 and 300 meters from shore. Here, alongshore velocities go to zero, and there is a reversal in the direction of the cross shore velocity at the surface and at depth (Figs. 13 and 12, middle, respectively).

When the typical wave transformation model (neglecting the wave roller) is applied to the Deep Bar Test Case, the results are similar to the results of the Shallow Bar Test Case. In the cross shore current, we see in Fig. 14 (top) a surface offshore flow from the seaward extent of the domain to about 430 meters from shore. At this point, the surface flow reverses to an onshore flow, and we note an area between 250-300 meters from shore where the surface cross shore current approaches zero. In Fig. 15 (top), we see the alongshore current form on the seaward slope of the bar near 410

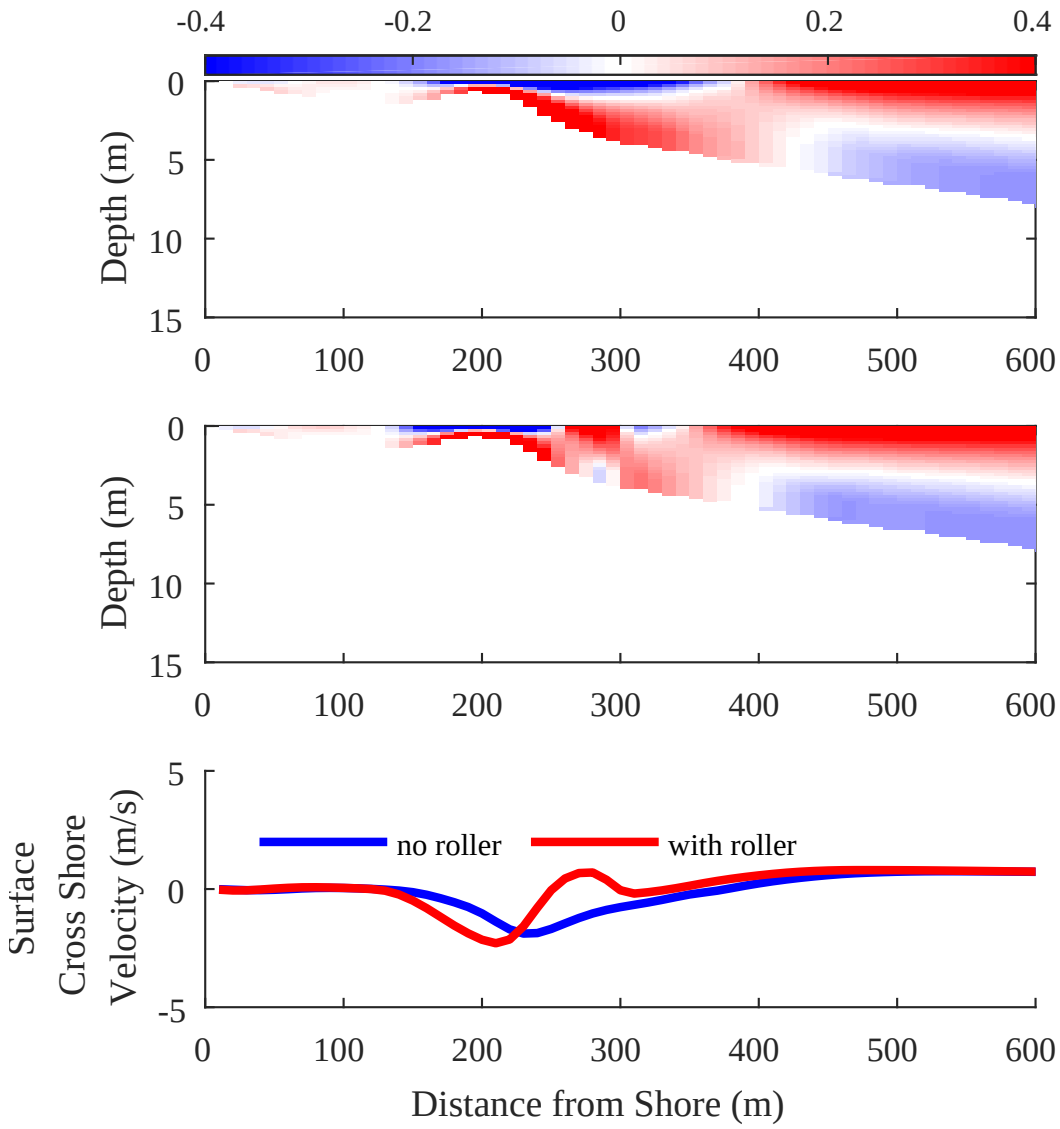

Fig. 12—Shallow Bar Test Case cross shore current slices over depth without (top) and with (middle) the wave roller approximation, where red indicates offshore flow and blue indicates onshore flow, and a comparison of the surface cross shore current profile with and without the wave roller approximation (bottom).

meters from shore. The current persists from the point of formation to very near the shore, with an area between 200-300 meters from shore exhibiting a relaxed current. Maximum values occur near the surface and decrease with depth. When the wave roller approximation is included, the initial reversal from offshore to onshore flow in the cross shore velocity moves shoreward approximately 20 meters (Fig. 14, middle). As in the Shallow Bar Test Case, we see a discontinuity between 250-300 meters from shore. In the Deep Bar Test Case, the discontinuity is shoreward of the bar. A discontinuity in the alongshore current, where the current goes to zero, is seen in the same area (Fig. 15, middle). Despite the discontinuity in the alongshore current profile, including the

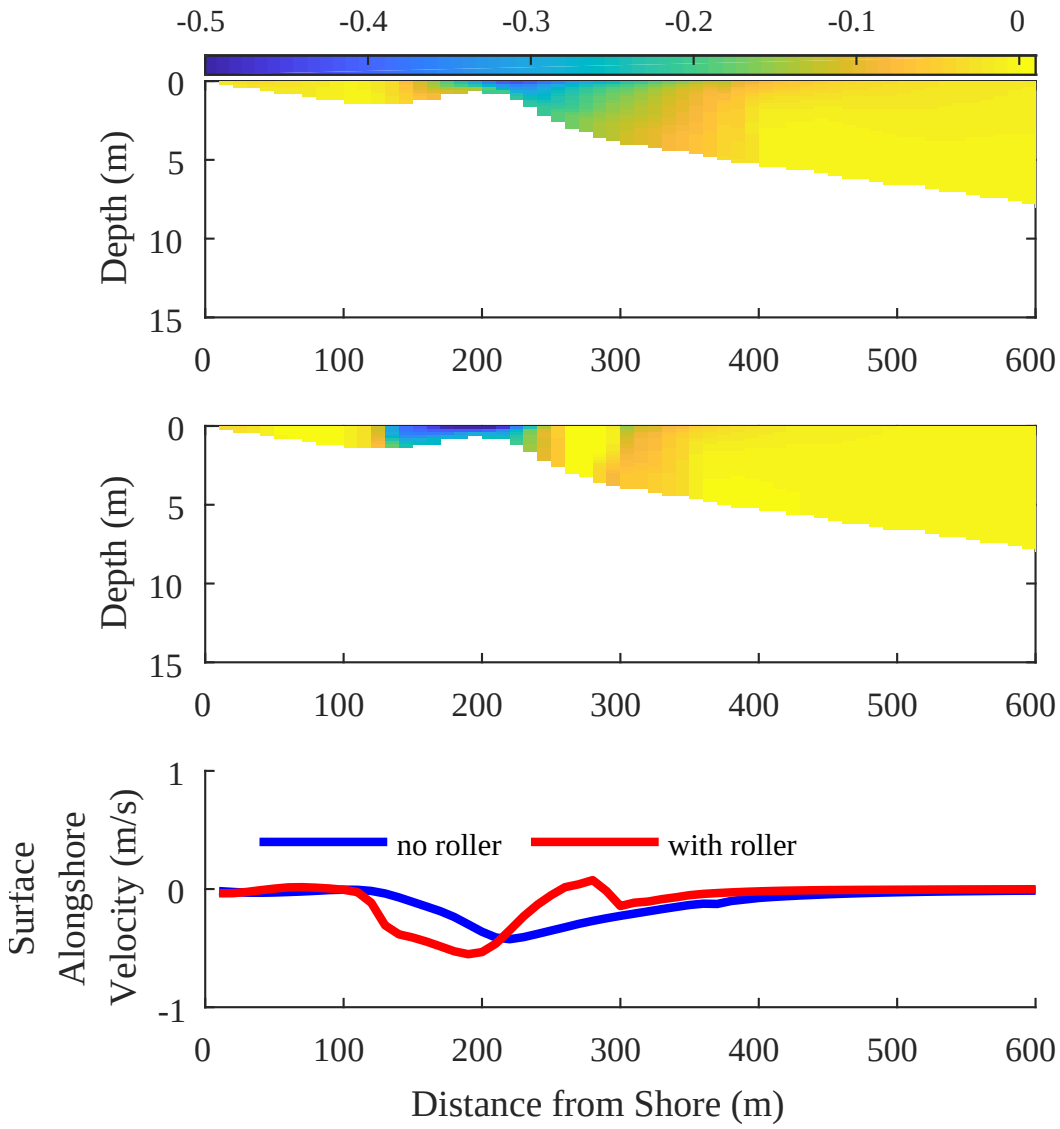

Fig. 13—Shallow Bar Test Case alongshore current slices over depth without (top) and with (middle) the wave roller approximation, and a comparison of the surface alongshore current profile with and without the wave roller approximation (bottom).

wave roller approximation generates a persistent, broad peak in the bar trough consistent with the findings of Smith et al. (1993) (Fig. 15, bottom).

3.4.2 Field Test Case

Because the 10-12 October 1994 time period includes waves approaching the beach at an oblique angle, we expect the waves to drive a strong along shore current at the surface. To analyze the results from this period, we focus on October 11, 1994 04:00. During this time, strong, oblique waves drove along shore currents in excess of 1 m/s, although surface measurements of currents do not exist to confirm these modeled values.

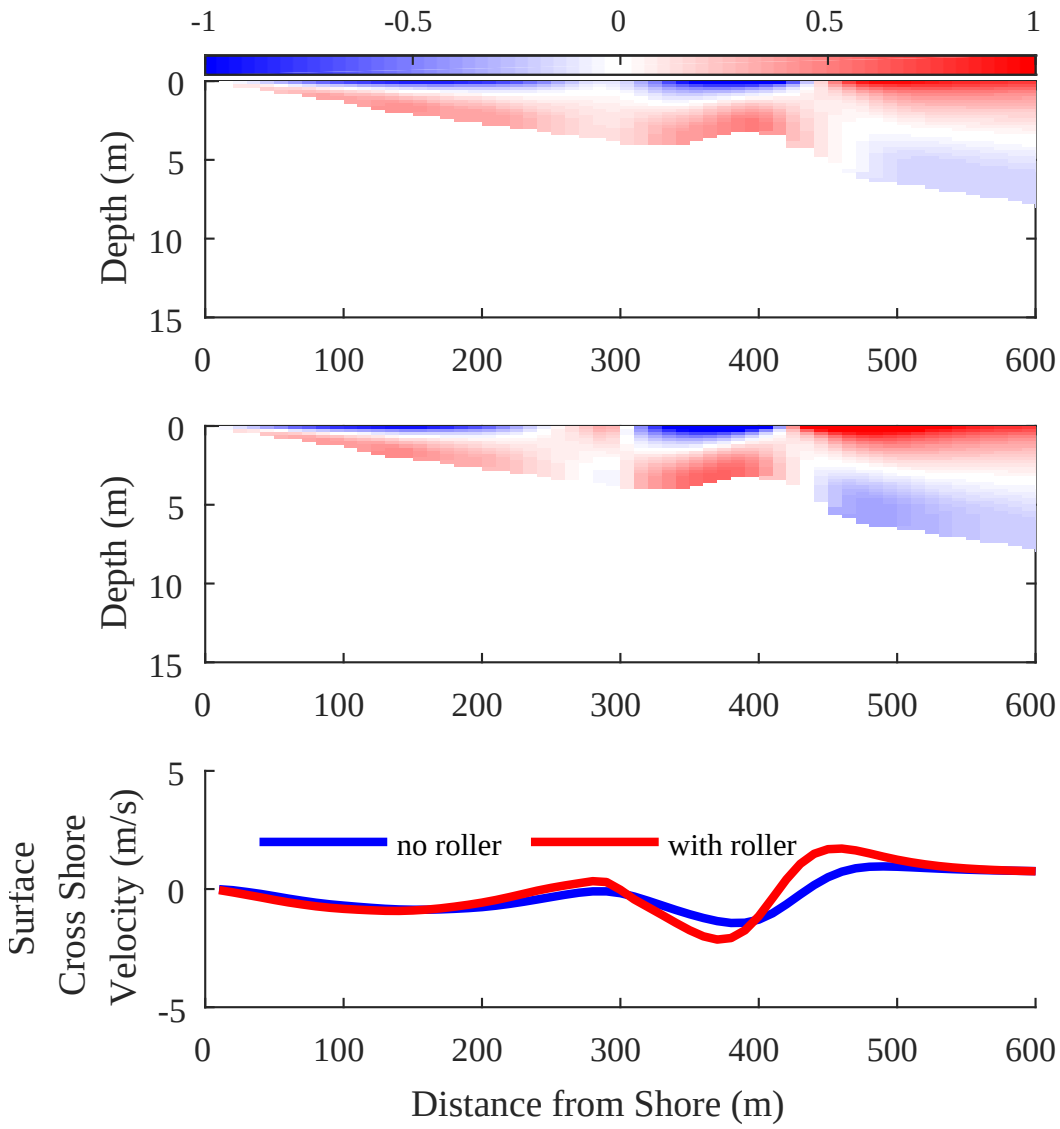

Fig. 14—Deep Bar Test Case cross shore current slices over depth without (top) and with (middle) the wave roller approximation, where red indicates offshore flow and blue indicates onshore flow, and a comparison of the surface cross shore current profile with and without the wave roller approximation (bottom).

At the surface, when the roller approximation is neglected, we see a continuous increase in the along shore current in the modeled surface layer. The current peaks just seaward of the bar crest. When the roller approximation is applied, we see the peak of the along shore current in the surface layer broaden and shift shoreward of the bar crest (Fig. 16, bottom). In addition, as with the idealized test cases, we see a discontinuity (a decrease) in the velocity seaward of the bar crest (Fig. 16, middle and bottom). Unlike the idealized test cases, the discontinuity does not result in an area with no along shore current or, worse, an area where the current flows in the opposite direction than expected.

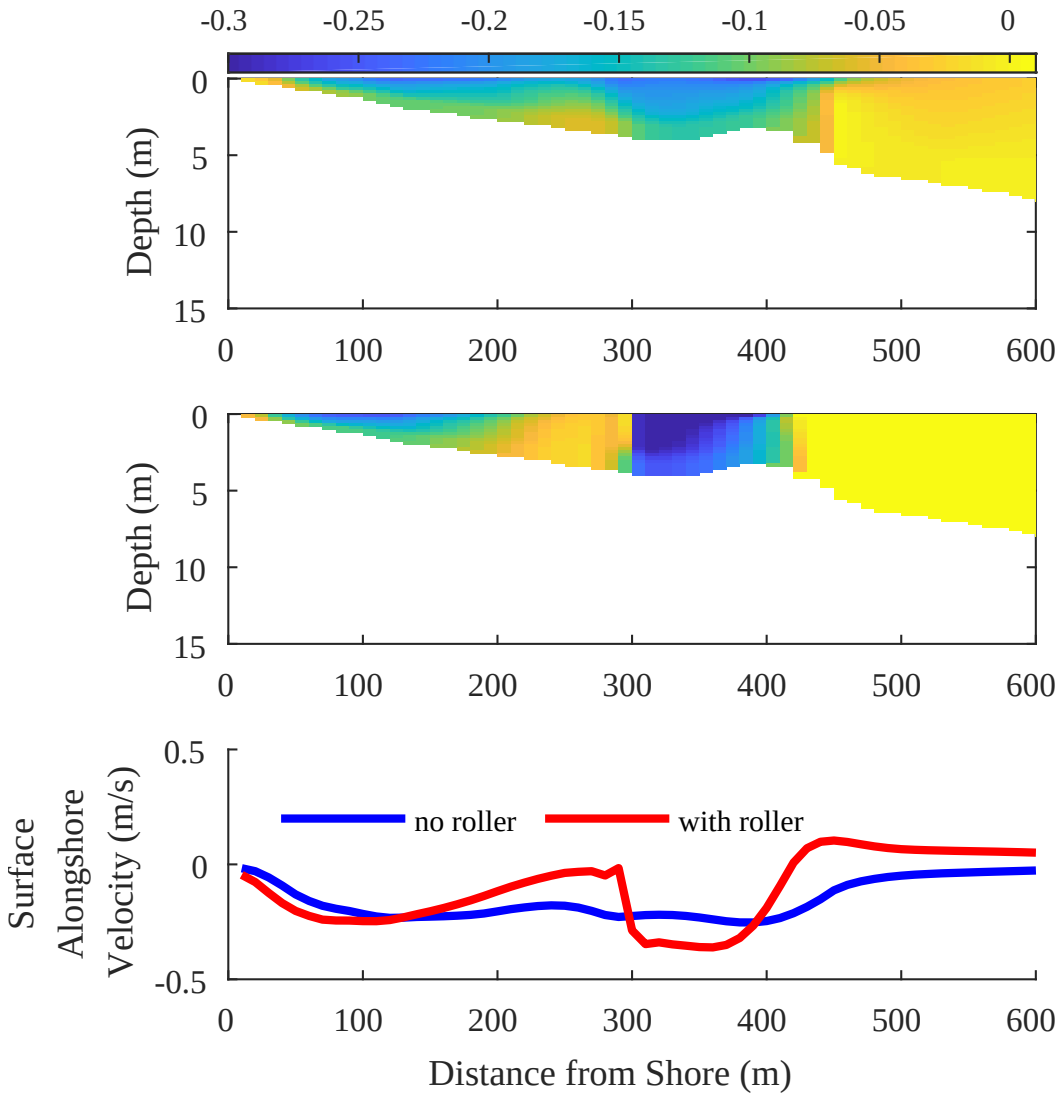

Fig. 15—Deep Bar Test Case alongshore current slices over depth without (top) and with (middle) the wave roller approximation, and a comparison of the surface alongshore current profile with and without the wave roller approximation (bottom).

Comparing the top and middle plots of Fig. 16 shows that including the roller approximation extends the highest values of along shore current (1 m/s or greater) deeper into the water column in the bar trough (near the 200 meter cross shore location). This helps improve the model-data comparison at cross shore locations close to the bar crest. Furthermore, we see that seaward of the bar at a location 370 meters from shore where multiple measurements are taken in the water column, the model results excluding and including (Figs. 17 and 18, respectively) the rollerapproximation are more variable than the measurements. On the contrary, shoreward of the bar, approximately 190 meters from shore, the measured currents vary more with depth than the modeled currents (Figs. 17 and 18).

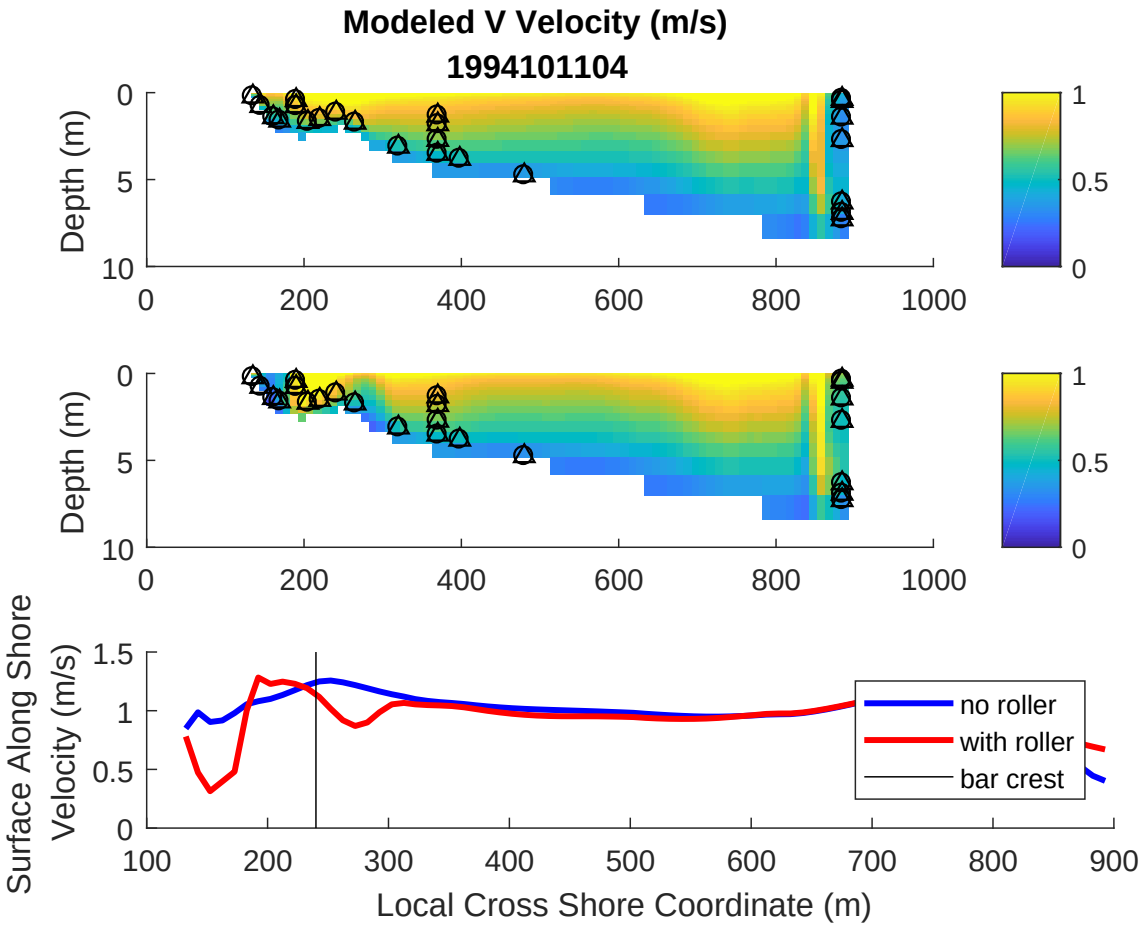

Fig. 16—Cross shore profiles of modeled along shore velocity. The figure shows a cross shore-depth slice of along shore velocity neglecting the roller approximation and including the roller approximation (top and middle, respectively) and a cross shore profile plot of along shore velocity in the surface layer of the model (bottom) neglecting and including (blue and red, repectively) the roller approximation. In the top and middle plots, the circles and triangles mark the in situ measurement locaitons. In the bottom plot, the black vertical line marks the location of the bar crest.

The measured peak in along shore current is formed by the measurements taken 205, 220, 241, and 265 meters from shore (Figs. 17 and 18). The highest along shore current is measured at 220 meters from shore—slightly shoreward of the bar peak, which is 240 meters from shore, and it is slightly greater than the measurement taken at 241 meters from shore. We will focus on these four cross shore locations for the model-data comparison of along shore velocity remembering that these are not surface measurements.

265 meters from shore, the model without the roller approximation compares well with the data (Fig. 17). However, when the roller approximation is applied, this measurement location is affected by the discontinuity in the modeled along shore velocity. The discontinuity is more evident near the bottom of the water column (Fig. 16, middle), and the modeled velocity at this location decreases from about 0.6 m/s without the roller approximation to about 0.4 m/s with the approximation (Figs. 17 and 18, respectively).

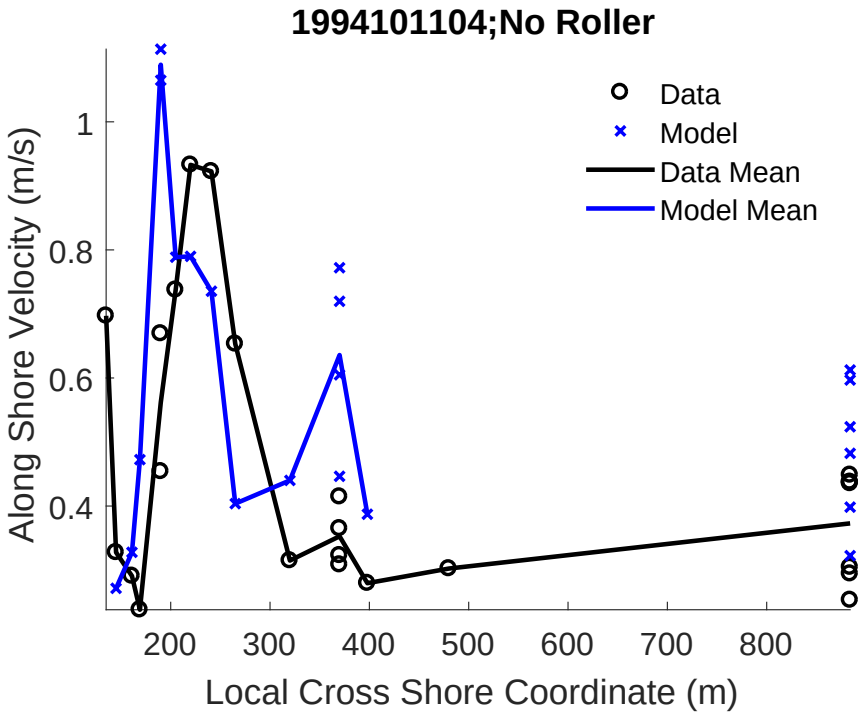

Fig. 17—Model-data comparison of along shore velocity magnitude. The model (blue) excludes the roller approximation. The black marks indicate along shore velocity measurements taken at cross shore locations. As shown in Fig. 16, at several cross shore locations, multiple measurements are taken at varying depths in the water column. The black line indicates the depth average of the along shore current measurements. The blue marks indicate the model results at the measurement locations with respect to cross shore location and depth. The blue line is the average of the blue marks.

Near the bar crest, at the measurement location 241 meters from shore, the along shore velocities generated by the models with and without the roller approximation are similar in value. In both instances, the model under estimates the measured along shore velocity by more than 0.1 m/s (Figs. 17 and 18) .

It is at the two measurement locations shoreward of the bar crest (220 and 205 meters from shore) that we see the greatest benefit of the roller approximation. Just shoreward of the bar crest at a location 220 meters from shore, neglecting the roller effects underestimates the along shore current by more than 0.2 m/s (Fig. 17). When the roller approximation is included in the model, the along shore velocity prediction increases by about 0.1 m/s, improving but still under predicting the measurement (Fig. 18). 205 meters from shore, the model without the roller approximation underestimates the measured along shore velocity by more than 0.1 m/s (Fig. 17). When the roller approximation is included in the model, the predicted along shore velocity increases becoming more agreeable to the measurement at this location over estimating it only slightly (Fig. 18). It is important to remember that we are comparing locations in the water column, not at the surface.

Just shoreward of the four measurement locations that form the peak of the along shore velocity at a location 190 meters from shore, measurements are taken closer to the surface. At this location, both models (with and without the roller approximation) greatly overestimate the along shore

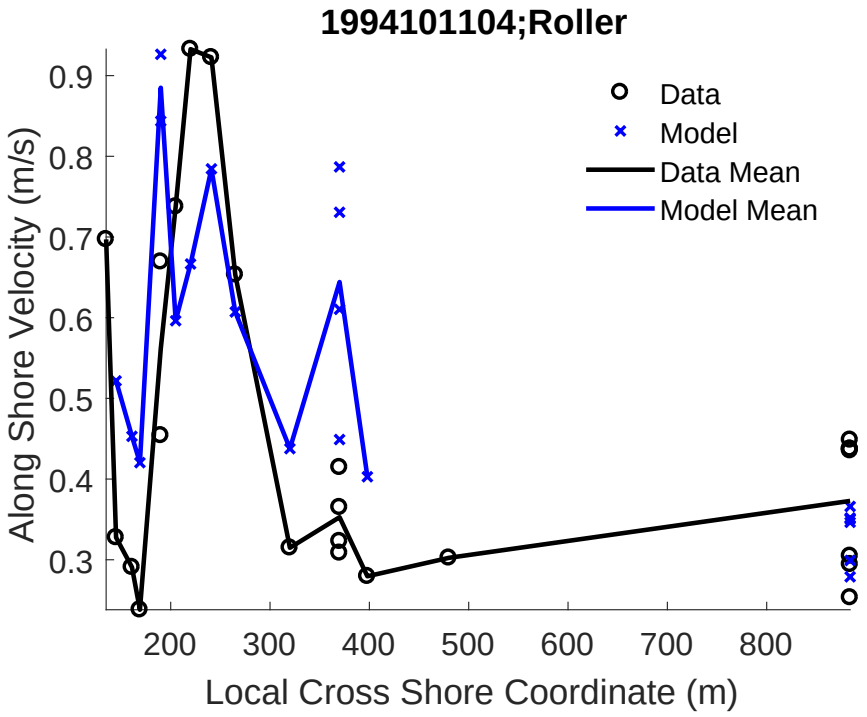

Fig. 18—Model-data comparison of along shore velocity magnitude. The model (blue) includes the roller approximation. The black marks indicate along shore velocity measurements taken at cross shore locations. As shown in Fig. 16, at several cross shore locations, multiple measurements are taken at varying depths in the water column. The black line indicates the depth average of the along shore current measurements. The blue marks indicate the model results at the measurement locations with respect to cross shore location and depth. The blue line is the average of the blue marks.

velocity. The data-model difference is more than 0.3 m/s without the roller approximation and more than 0.6 m/s with the roller approximation (Figs. 17 and 18, respectively).

At the shallowest measurement locations, the model without the roller approximation overestimates the along shore velocity (Fig. 17). With the roller approximation, the model is in better agreement with the data (Fig. 18).

3.5 Summary of Wave Roller Approximation

A wave roller approximation was formulated and applied to the COAMPS modeling system. The system was configured for two test cases–an idealized test case that considers a plane beach bathymetric surface and two parameterized barred bathymetric surfaces and a field test case. The field test case at Duck, North Carolina was part of the validation test for the current operational nearshore system.

Over three different bathymetric surfaces, the idealized test case shows that the roller approximation is capable of producing the effects of the wave roller. The approximation moves the peak along shore current shoreward, increasing the current magnitude and broadening the peak. However, when a bar is present in the bathymetric surface, a discontinuity forms in the velocity

predictions. Further investigation leads to a numerical explanation of the discontinuities. As waves approach a bathymetric bar, the radiation stresses determined by the roller approximation increase, and shoreward of the bar, the radiation stresses decrease forming maxima in the calculated radiation stresses. Gradients of the radiation stresses produce the wave forcing, and derivatives at points of inflection are zero. Therefore, the wave forces at the maxima of radiation stress are zero producing a discontinuity in the resulting velocities.

The field test cases, which include bathymetric bars, results in velocity discontinuities similar to the discontinuties of the idealized test case. It is shown that including the roller approximation does not effect model efficiency. However, we note (although not reported in the results) that for the field test case presented, the COAMPS system is less efficient than the current operational system for predicting surf zone hydrodynamics, including wave induced currents.

4. WAVE FORCING USING DISSIPATION

Since the introduction of the wave radiation stress gradient (WRSG) concept (Longuet-Higgins and Stewart, 1962), it has been the primary mechanism by which wave momentum is applied to hydrodynamic models in order to drive wave-induced circulation. As long as the waves are resolved with sufficiently high grid resolution and there is no wave generation within the domain, i.e. the waves primarily enter the domain from the boundary, the modeled wave-driven circulation has high fidelity. However, if the winds are strong and the domain large enough to generate waves inside the domain, the magnitude of the momentum transferred from the waves to the ocean will typically be in error. The primary reason for this erroneous momentum transfer is that the radiation stress gradients are calculated as a function of the change in wave energy (i.e. change in wave height). In the situation where there is a balance between waves breaking and waves generated, such that the overall wave energy remains constant, then, as per radiation stress gradient calculations, there will be no momentum transfer from waves to the ocean. Another issue arises as a result of course grid resolution. If the resolution is too coarse to capture WRSG changes due to wave breaking, especially in shallow nearshore waters and along the shoreline, artifacts in the WRSG field are introduced giving rise to artificial currents and/or numerical instabilities.

To avoid these issues, Dingemans et al., (1987) proposed using wave dissipation as the mechanism to transfer momentum from waves to the ocean. The methodology is similar to the vortex force formulation, later derived by McWilliams et al. (2004) and implemented by Kumar et al. (2012), in which the conservative and non-conservative effects of waves on currents are represented.

4.1 Description of Wave Dissipation Forcing

The wave dissipation-based calculation of momentum transfer within COAMPS uses the formulation of Tang et al. (2004). The momentum equations in the ocean model, NCOM, relevant to this implementation, are given in Cartesian coordinates as:

$$\frac{D\mathbf{u}}{Dt} = \ldots + \mathbf{F_w} \tag{17}$$

where boldface letters indicate vector quantities with $\mathbf{u}$ the horizontal velocity vector and F_w the vector wave forcing. For the wave radiation stress gradient formulation,

$$\mathbf{F_w} = \nabla \iint \left[n \cos\theta^2 + n - 0.5 \right] E(\sigma, \theta)\, \mathrm{d}\sigma\, \mathrm{d}\theta \tag{18}$$

For the wave dissipation formulation,

$$\mathbf{F_w} = -\frac{1}{\pi} \iint \sigma \hat{\mathbf{k}} k S_{ds} e^{2kz}\, \mathrm{d}\sigma\, \mathrm{d}\theta \tag{19}$$

where σ is the relative wave frequency, $\hat{\mathbf{k}}$ is the unit vector in the direction of wavenumber $\mathbf{k}$, θ is the wave direction, and S_{ds} is the source term for wave dissipation, as computed in SWAN. The SWAN model solves the wave action balance equation as:

$$\frac{\partial N}{\partial t} + \nabla_{\mathbf{x}} \cdot [(\mathbf{c_g} + \mathbf{u}_s) N] + \frac{\partial c_\sigma}{\partial \sigma} + \frac{\partial c_\theta}{\partial \theta} = S_{in} + S_{ds} + S_{nl} \tag{20}$$

where $N(f, \theta) = E(f, \theta)/\sigma$ is the wave action, $E(f, \theta)$ is the wave energy, c_g is the group velocity, $\mathbf{u}_s$ is the surface horizontal velocity vector, and c_σ and c_θ are the wave propagation velocities in frequency and direction space, respectively. The source terms for wave generation and wave dissipation are given as S_{in} and S_{ds}, respectively, and S_{nl} is the source term for non-linear wave interactions.

4.2 Test Cases and Model Configuration Used to Evaluate Wave Dissipation Forcing

To validate implementation of the wave dissipation forcing within COAMPS, two current operational areas were selected. The larger, coarse resolution domain is the US East domain (Figure 19a). For the ocean model, NCOM, the grid resolution is 0.03333° in both the latitude and longitude directions with a total grid size of 18.13°× 22.13° (544 nodes in longitude and 664 in latitude). There are 49 vertical layers, with the top 35 being σ layers (bathymetry following) whose resolution is concentrated at the ocean surface and the remainder are fixed z-levels extending to ocean bottom. The temporal resolution (time step) is 12 seconds. Atmospheric boundary conditions are provided by the COAMPS atmospheric model. Along the open ocean boundary, water surface elevation, currents, temperature and salinity are extracted from the HYCOM global ocean model. Wave information comes from the SWAN wave model which is defined over a slightly larger area (18.2°× 22.2°) at a lower resolution of 0.1°. The wave model is run with a 6 minute time step.

The second, high resolution domain, labeled “Chesapeake Bay” is a nested subdomain of US East, centered at Chesapeake Bay and shown in Figure 19b. For this domain, the NCOM grid resolution of 0.0045° is uniform in both latutude and longitude. The size of the Chesapeake domain is 4.8915°×4.995° (1087 nodes in longitude and 1111 in latitude). Due to the higher spatial resolution, 50 vertical layers are prescribed, with the top 30 being σ layers (bathymetry following) and the remainder fixed z-levels spanning the deep ocean. The temporal resolution (time step) is 4 seconds.

Similar to US East, atmospheric boundary conditions are provided by the COAMPS atmospheric model. Alternatively, forcing along the open ocean boundary, including water surface elevation, currents, temperature and salinity, are obtained from the US East simulations. The SWAN wave model again is configured for a slightly larger area compared to the ocean model ($4.9005^\circ \times 22.2^\circ$) at a lower resolution of 0.0135°. The wave model is run with a 5 minute time step.

Wave forcing for both the US East and Chesapeake Bay domains consisted of the original WRSG formulation, Eq. (18) described previously in Section 2, as well as the new wave dissipation (WD) formulation, Eq. (19). The simulation period for the US East model extended nearly 12 months from Jan 01, 2015 0000 UTC to Dec 12, 2015, 2400 UTC. For Chesapeake Bay, the same simulation period was selected, though starting two weeks later to allow spinup of the US East domain. The exact simulation period for Chesapeake Bay was then Jan 15, 2015 0000 UTC to Dec 12, 2015, 2400 UTC. For both domains, the simulation cycle started each day at 0000 UTC, with data assimilated from 0000 UTC to 1200 UTC and run in forecast mode from 1200UTC to 2400 UTC. All comparisons presented here use results from the forecast period of the simulation only.

4.3 Results From Testing Wave Dissipation Forcing

For US East, observations of water levels and currents are sparse; if available they are limited to coastal areas which are coarsely resolved within this domain. However, data are available for temperature and salinity from a variety of sources throughout the domain, including National Data Buoy Center moored buoys, miltary Training and Evaluation System for Active Countermeasures (TESACs), expendable bathythermographs (XBTs), and Argo floats which have been collected and quality controlled by NAVOCEANO. Altimeter data are also available for significant wave heights.

First we examine scatter plots for significant wave height over the US East region (Figure 20). The statistics show marginal improvement using the WD formulation (Fig. 20b) over the WRSG approach (Fig. 20a), but the differences are not statistically significant. Similarly, comparison of the salinity profiles from 2m below mean water level to 200m water depth (Figure 21) and temperature profiles over the same depth range (Figure 22) show similar results statistically. We chose to limit comparisons to the upper 200m since wave effects rarely reach deeper into the ocean, and both wave forcing formulations show nearly identical values below the 200m level.

To consider seasonal statistical differences during the year, we look at profiles during the period Jan 1 - March 31 (Figures 23 and 24), April 1 - June 30 (Figures 25 and 26), July 1 - September 30 (Figures 27 and 28), and October 1 - December 31 (Figures 29 and 30). During the first quarter of the year, though salinity profiles are nearly identical to each other, the WD formulation does far better in predicting water temperature. During the second quarter, the WD method results in a slightly lower root mean square error (RMSE) for salinity, but mean errors for the two methods are nearly the same. For temperature during the same period, the RMSE is smaller for the WD formulation in the upper 100m, but larger in the lower 100m. Mean error (ME) in temperature is reduced for the WD formulation compared to that of the WRSG approach over the entire vertical range. The results change a bit in the third quarter when salinity profile errors (RMSE and ME) for the WRSG method are both less than those of the WD formulation. A more varied result is seen for the temperature profiles. The RMSE for the WRSG formulation is less than that of the WD method, but for ME the opposite is true; the WD formulation ME is less than that of the WRSG approach. In the fourth quarter, the RMSE for both salinity and temperature is smaller for

the WRSG method in the top 100m, but the result is reversed over the 100-200m range. The ME for salinity is very similar for both formulations, but for temperature, the WRSG method provides better results even though the value of the average ME over the entire vertical range is slightly less for the WD formulation.

Next, we consider results from the Chesapeake Bay high resolution simulation. The significant wave heights (Figure 31) indicate that the WD approach yields a marginally better performance as measured by all computed statistical quantities. However, there is no such indication for salinity (Figure 32) or temperatiure (Figure 33). The magnitude of the errors (RMSE and ME) for the Chesapeake Bay domain are on the whole larger that those computed for the US East domain, regardless of which formulation is used. Whereas the differences seen in significant wave heights are minor, the differences for salinity are moderately high, and for temperature significantly higher. For the temperature profiles, errors are concentrated at the surface down to the mixed layer depth (approximately 50m depth). To reiterate, the computed deviation from observations for both temperature and salinity is unaffected by the formulation of momentum flux transfer used, which implies that some underlying phenomena is not being accounted for in the model physics. A large portion of this error could be attributed to how the river flux into the bay is implemented within COAMPS. River fluxes are derived from a coarse, static, monthly mean climatology, which neglects the synoptic meteorological influences on the region. Near-future COAMPS transitions will address this known shortcoming.

Given the higher resolutions of the Chesapeake Bay test case solutions, water level comparisons between simulations using the WRSG and WD methods are appropriate. Four stations in Virginia having water level observations are listed in Table 2. Water level comparisons to observations (black) are shown in Figure 34 for the WD (blue) and WRSG (red) formulations. Both wave forcing formulations yield very similar water level phasing but exhibit a large negative bias in magnitude at all locations. The biases for each wave forcing formulation (WD and WRSG) are provided in Table 2. These biases originate from the applied water level boundary conditions derived from the larger US East model solution. Accuracy of the tides in coastal waters of the US East model is sub-optimal due to its coarser spatial resolution and application of an outdated tidal database at its open ocean boundary. Removing the water level biases from Chesapeake Bay model solutions yield a better correlation between simulated and observed water levels as seen in Figure 35. However, the models do not show the same tidal range as the data. This is more obvious from Figure 36, which shows a scatter plot of water levels with the bias removed (water level (m) vs. time), where we see that the modeled results exhibit larger values at low tide and smaller values at high tide.

4.4 Three Case Studies Within the Test Period

Three case studies from the US East domain simulations span time frames that coincide with the occurance of specific meteorological events. These three events are selected because of the significant wind energy present in the domain. They include the January 2015 North American Blizzard and Hurricanes Joaquin (September 2015) and Kate (November 2015). For each of these case studies, observations at the same four water level stations in Virginia listed in Table 2 are examined, Sewell's Point, Chesapeake Bay Tunnel, Kiptopeke Beach, and Yorktown. For simulations using both the WD and WRSG formulations, time series of water levels vs. observations and scatter plots of observed (x-axis) vs. modeled (y-axis) water levels are presented. For each simulation, results are shown with and without the computed biases of Table 2 removed.

Table 2—Model biases for WD and WRSG forcing at all water level stations

Name (ID)	Latitude (°W)	Longitude (°W)	Bias (Dissipation) (m)	Bias (Radiation Stress) (m)
Sewells Point, VA (8638610)	36.9467	76.3300	-0.39	-0.39
Chesapeake Tunnel, VA (8638863)	36.9667	76.1133	-0.42	-0.43
Kiptopeke Beach, VA (8632200)	37.1650	75.9883	-0.43	-0.43
Yorktown, VA (8637689)	37.2267	76.4783	-0.40	-0.40

4.4.1 The January 2015 North American Blizzard

On January 23, a low-pressure area developed off the Pacific Northwest, before moving over the Canadian Prairies by January 24. The storm system quickly moved southeastward into the Upper Midwest during the evening of January 24. Rapid eastward movement of the storm system led to a weakening by January 26. Concurrently, a low-pressure system that formed off the coast of North Carolina began to track north-northeastward, eventually becoming the dominant low of the system. The storm system persisted until around early January 30, moving out of the region by January 31. The lowest pressure measured during this period was 960 mb with 1-minute sustained winds of 75 mph (120 kmph) and gusts up to 95 mph (153 kmph) recorded.

Figures 37-40 compare observed water levels with computed water levels during the January Nor'easter at all four stations referenced in Table 2. Results with the biases removed (bottom panels) indicate that the US East model is able to reproduce general water level trends, with an especially good match of the phases. Water level magnitudes tend to have a smaller range than those of the observations. This error is most prominent at Yorktown while at Kiptopeke Beach and Sewell's Point the range is closer to the measurements. The best match between model and data are observed at Chesapeake Bay Tunnel. The model-data discrepancies between stations are likely due to the specific gage location. For example, the station at Chesapeake Bay Tunnel is located in open water while Sewell's Point is quite sheltered by the shoreline configuration. Unfortunately, the US East model resolution is not sufficient to precisely capture the dynamics at all of the station locations.

4.4.2 Hurricane Joaquin, September 2015

Hurricane Joaquin was the strongest hurricane of the 2015 Atlantic hurricane season, nearly reaching Category 5 status on the Saffir–Simpson scale with a maximum wind speed of 155 mph (135 kt) and a minimum central pressure of 931 hPa (Berg, 2016). Although the storm did not make landfall in the US, it was responsible for record-breaking rains and flooding across North and South Carolina. It also caused large waves and currents off the coast of North Carolina. Although

the North and South Carolina region is not contained in the Chesapeake Bay domain, the impact of Hurricane Joaquin was obvious in US East water levels.

Computed water levels during Hurricane Joaquin are compared to observed water levels in Figures 41-44 at all four stations referenced in Table 2. As for the previous case study, the two wave momentum transfer formulations (WD and WRSG) give near identical results. Notable is that water level magnitudes at the peak of the storm are substantially underpredicted. Such mismatches at the peak of the storm could be due to inaccuracies in the COAMPS atmospheric model representation or resolution of the wind field.

4.4.3 Hurricane Kate, November 2015

Hurricane Kate was unique in that it was the last hurricane to develop, late in the 2015 season (Avila, 2016). Kate formed into a tropical depression about 1800 UTC, November 8 and became a tropical storm by 0600 UTC, November 9. Kate reached hurricane status at 0000 UTC 11 November, and achieved peak intensity of 86 mph (75 kt) approximately 12 h later. Shortly thereafter, the hurricane encountered strong shear and cold waters, and transformed into an extratropical cyclone, dissipating by 1800 UTC 13 November. Although it did not threaten any land, Hurricane Joaquin did create higher than normal waves in the Atlantic ocean, hence the reason for its inclusion here as a case study.

As with the two prior case studies, no statistical differences arise between simulations applying WD vs. WRSG forcing. The model error arising from comparison to observations is much less for Hurricane Kate than Hurricane Joaquin, likely a result of the substantial variation in intensity between the two storms. Differences between model performnace at the stations follows the pattern observed for the January Nor'easter in that computations at Sewell's Point contain the largest water level error while the modeled solution at Chesapeake Bay Tunnel results in the highest level of accuracy.

4.5 Summary of Wave Dissipation Forcing

An evaluation is presented comparing significant wave heights, salinity and temperature profiles, and water levels for two forms of wave momentum flux transfer, a radiation stress gradient based formulation (WRSG) and a dissipation based formulation (WD). The formulation for wave momentum transfer takes place in the coupling between the wave module (SWAN) and the ocean module (NCOM) within COAMPS. The coupled ocean-wave system using each formulation, WRSG and WD, was run for two test cases, a large-scale regional domain (US East) and a high resolution, smaller coastal domain (Chesapekae Bay), nested within the US East domain. The models were run for the entire year of 2015. Model-data comparisons spanned the entire year as well as shorter 10-15 day periods for three specific case studies (January 2015 North American Blizzard, Hurricane Joaquin, September 2015, and Hurricane Kate, November 2015). Overall, the wave dissipation based method (WD) was more stable, and performed slightly better than the wave radiation stress gradient (WRSG) approach for temperature and salinity profiles. However, differences between the two methods of wave momentum transfer are essentially negligible for the various test cases studied, with no appreciable differences in significant wave height or water level.

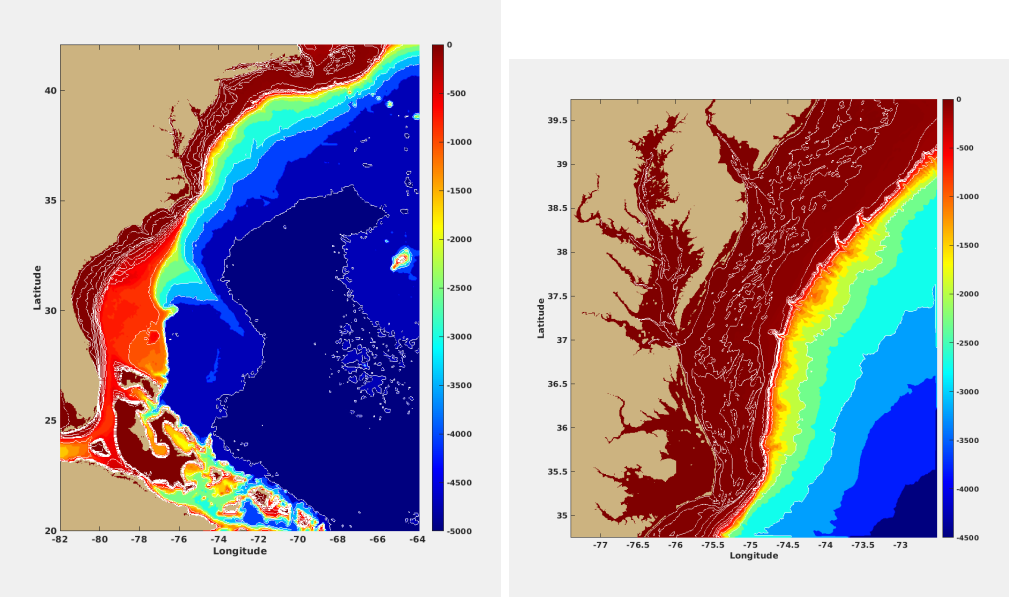

(a) US East (b) Chesapeake Bay

Fig. 19—Wave dissipation forcing test cases, domain and bathymetry, for operational regions (a) US East and (b) Cheasapeake Bay.

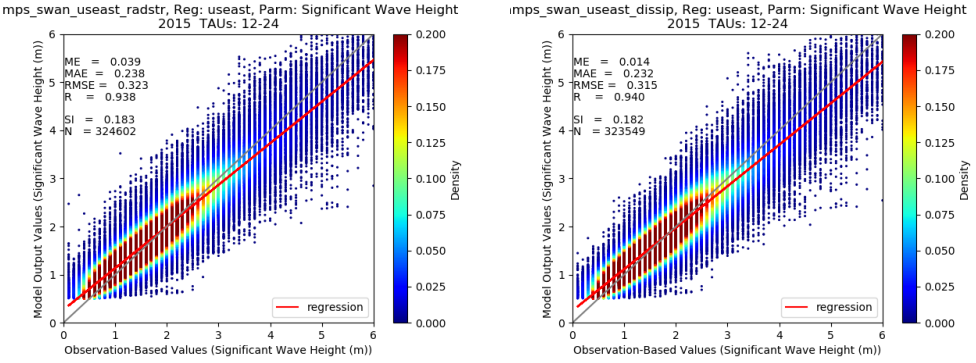

(a) Radiation Stress Gradient formulation (b) Dissipation formulation

Fig. 20—Significant wave height (m) comparisons, observed (x-axis) vs. modeled (y-axis), for the (a) WRSG and (b) WD formulations over the US East domain.

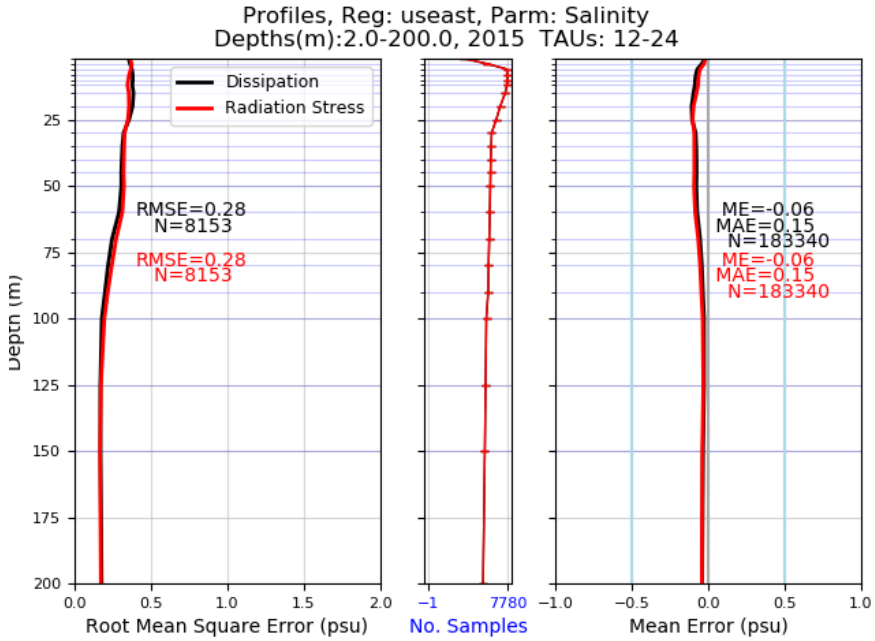

Fig. 21—Salinity Root Mean Square Error (left) and Mean Error (right) over depth for WD (black) and WRSG (red) formulations over the US East domain.

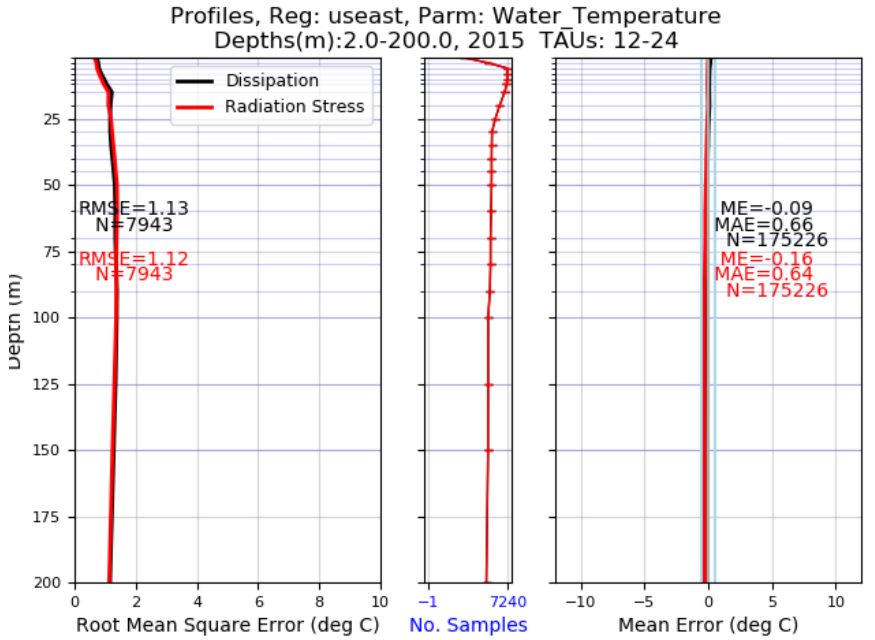

Fig. 22—Temperature Root Mean Square Error (left) and Mean Error (right) over depth for WD (black) and WRSG (red) formulations over the US East domain.

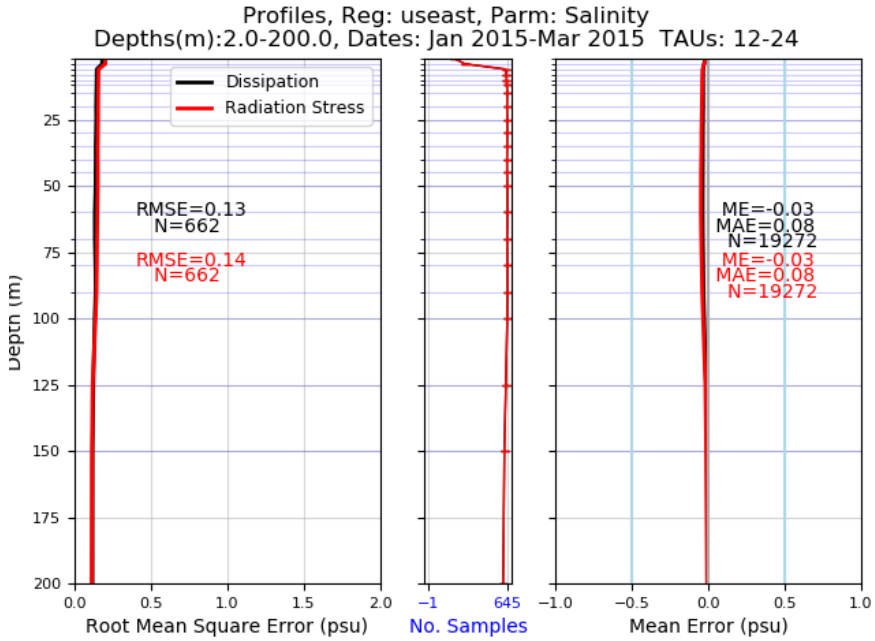

Fig. 23—Salinity (January 1 - March 31) Root Mean Square Error (left) and Mean Error (right) over depth for WD (black) and WRSG (red) formulations over the US East domain.

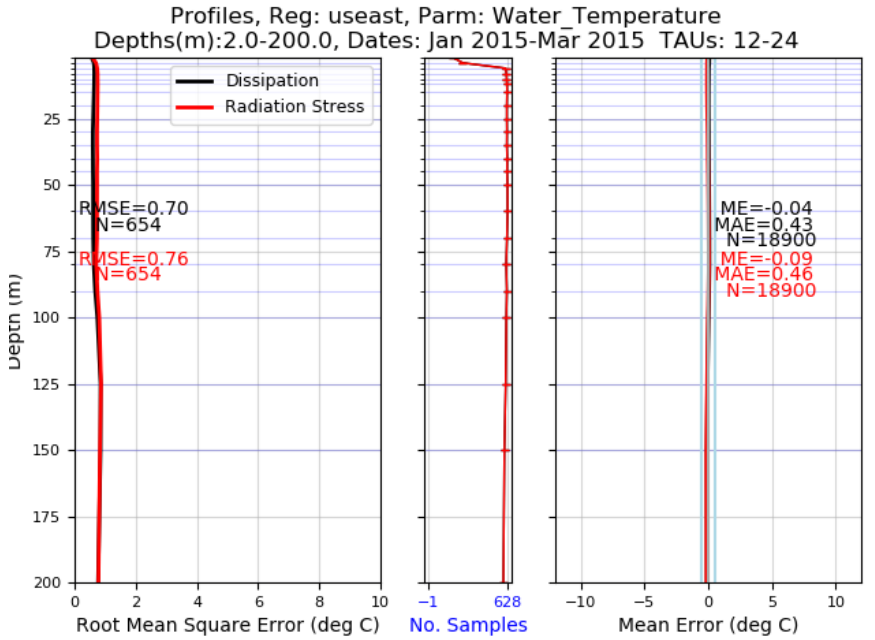

Fig. 24—Temperature (January 1 - March 31) Root Mean Square Error (left) and Mean Error (right) over depth for WD (black) and WRSG (red) formulations over the US East domain.

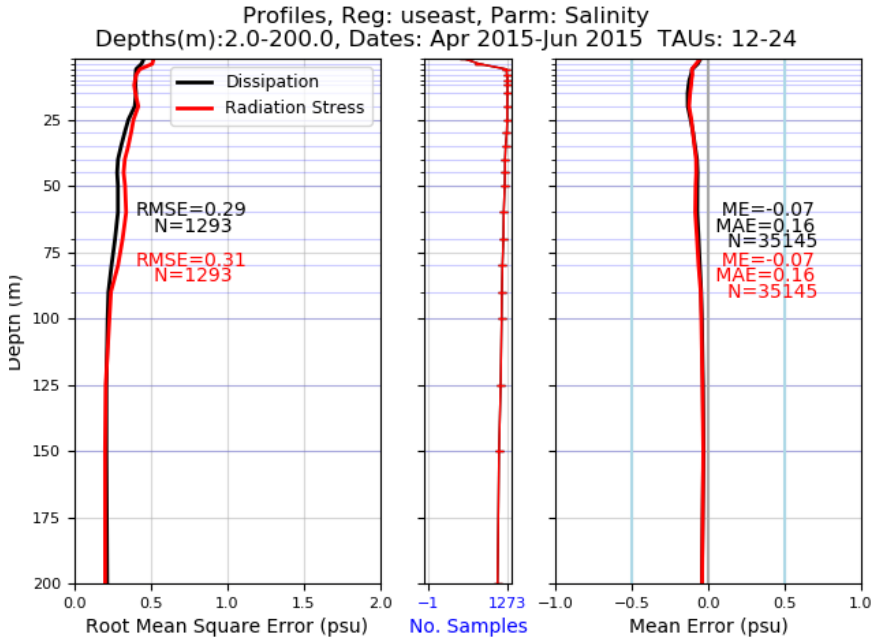

Fig. 25—Salinity (April 1 - June 30) Root Mean Square Error (left) and Mean Error (right) over depth for WD (black) and WRSG (red) formulations over the US East domain.

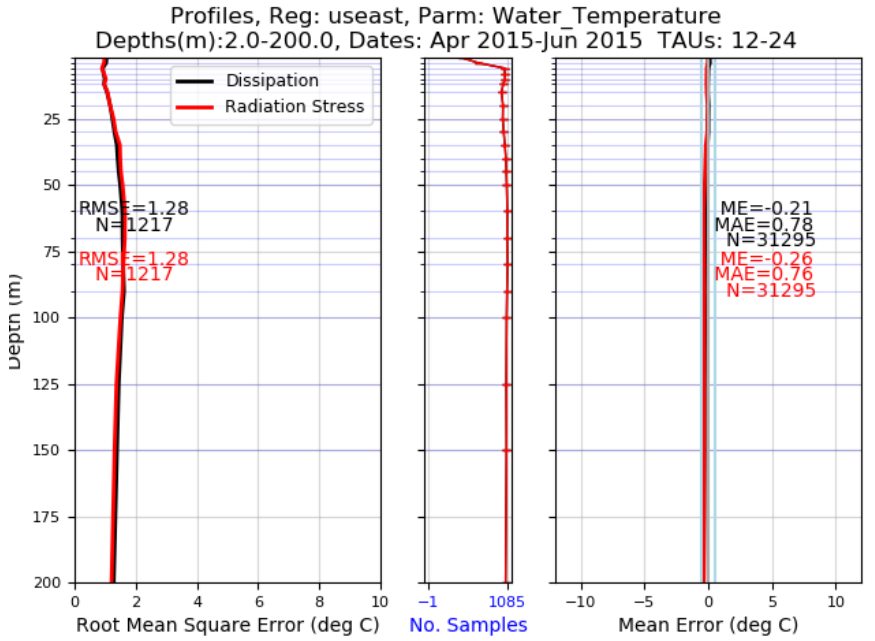

Fig. 26—Temperature (April 1 - June 30) Root Mean Square Error (left) and Mean Error (right) over depth for WD (black) and WRSG (red) formulations over the US East domain.

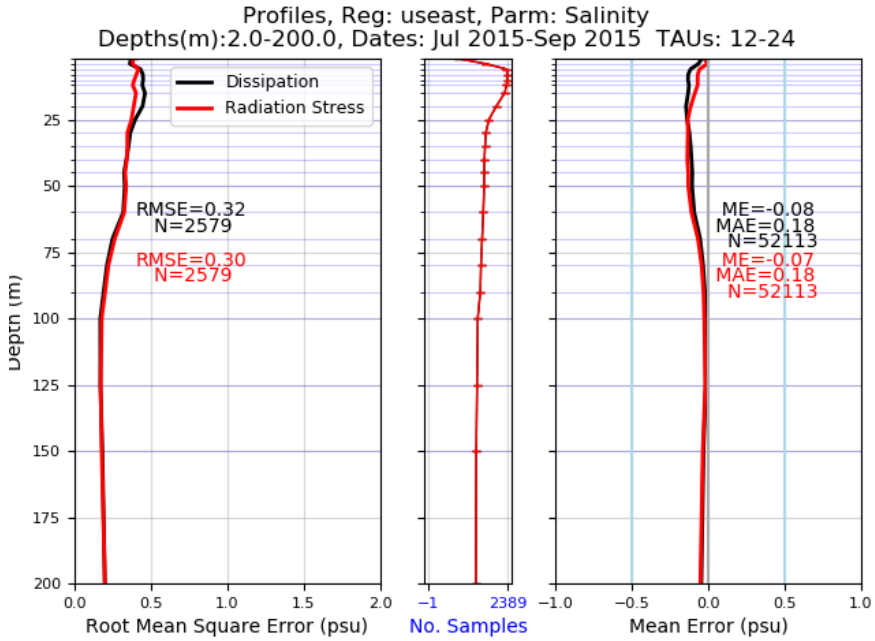

Fig. 27—Salinity (July 1 - September 30) Root Mean Square Error (left) and Mean Error (right) over depth for WD (black) and WRSG (red) formulations over the US East domain.

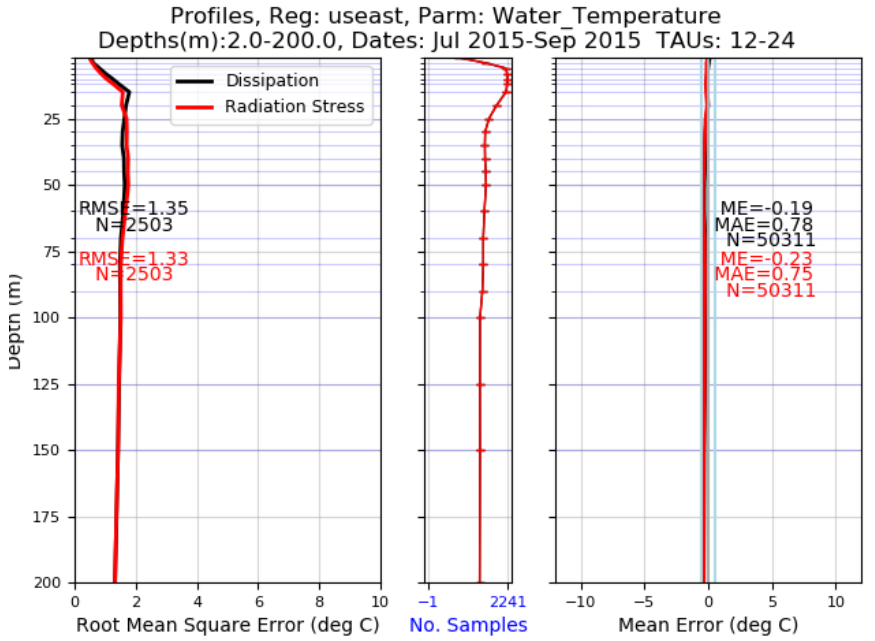

Fig. 28—Temperature (July 1 - September 30) Root Mean Square Error (left) and Mean Error (right) over depth for WD (black) and WRSG (red) formulations over the US East domain.

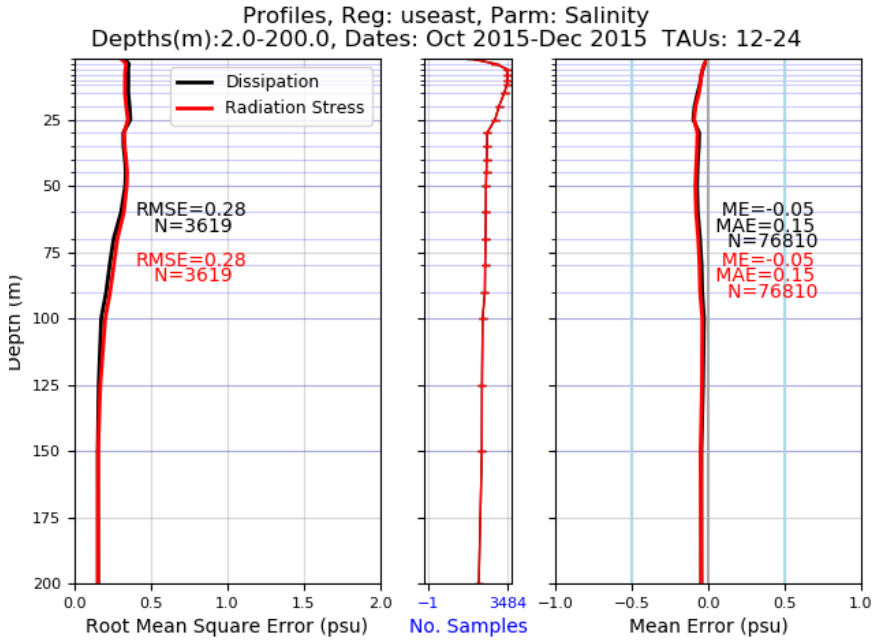

Fig. 29—Salinity (October 1 - December 31) Root Mean Square Error (left) and Mean Error (right) over depth for WD (black) and WRSG (red) formulations over the US East domain.

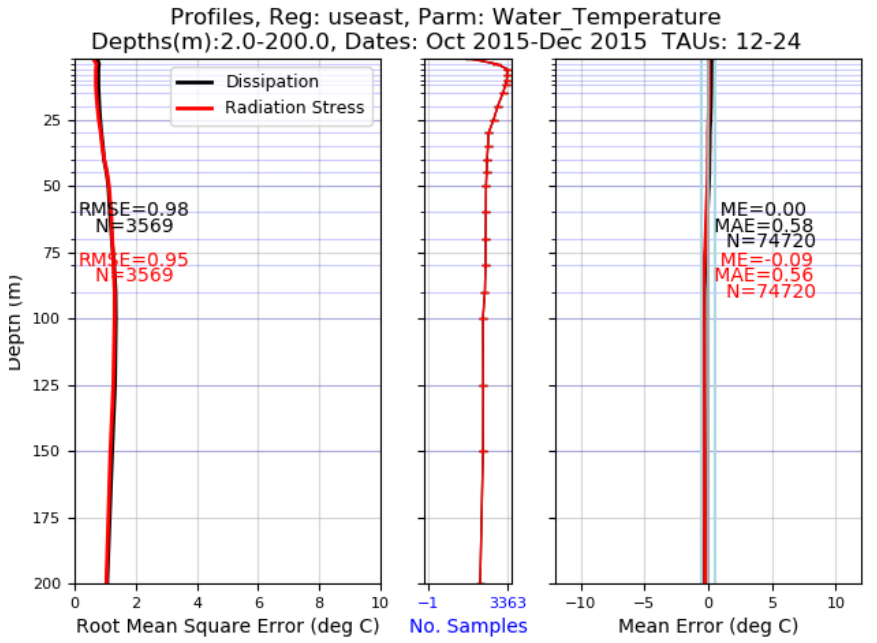

Fig. 30—Temperature (October 1 - December 31) Root Mean Square Error (left) and Mean Error (right) over depth for WD (black) and WRSG (red) formulations over the US East domain.

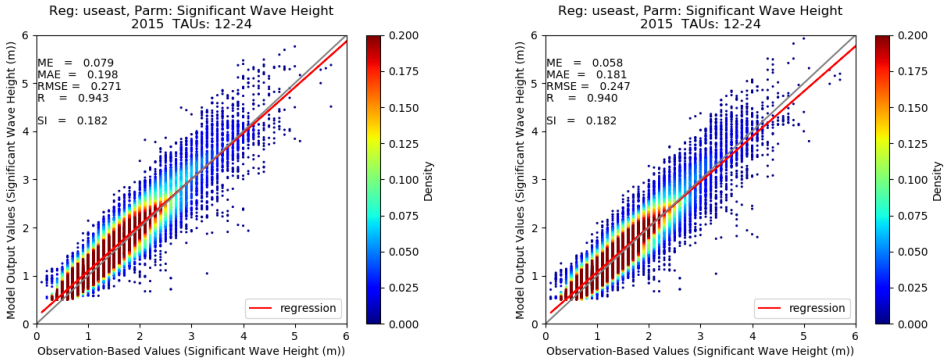

(a) Radiation Stress Gradient formulation (b) Dissipation formulation

Fig. 31—Significant wave height (m) comparisons, observed (x-axis) vs. modeled (y-axis), for the (a) WRSG and (b) WD formulations over the Chesapeake Bay domain.

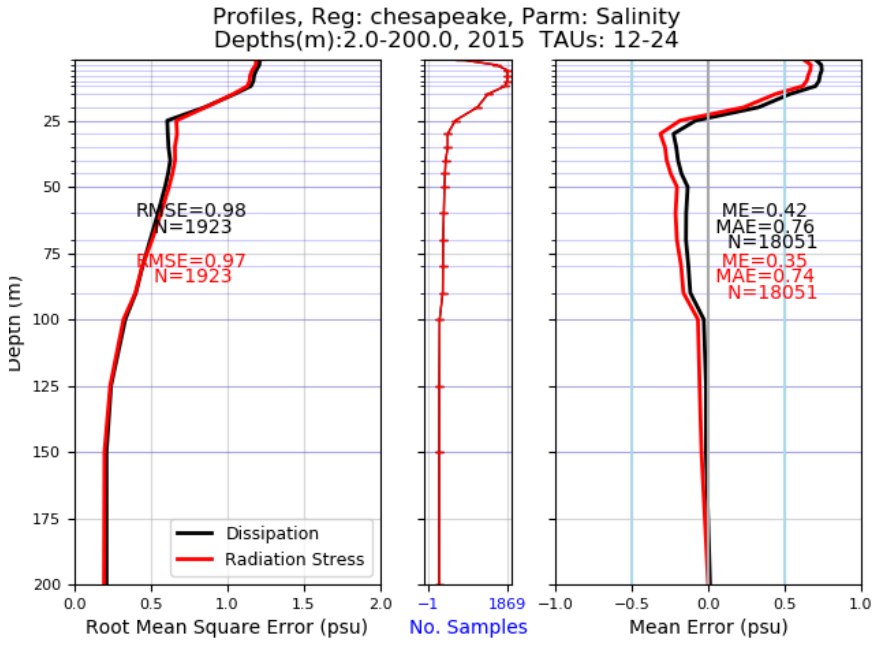

Fig. 32—Salinity Root Mean Square Error (left) and Mean Error (right) for WD (black) and WRSG (red) formulations over the Chesapeake Bay domain.

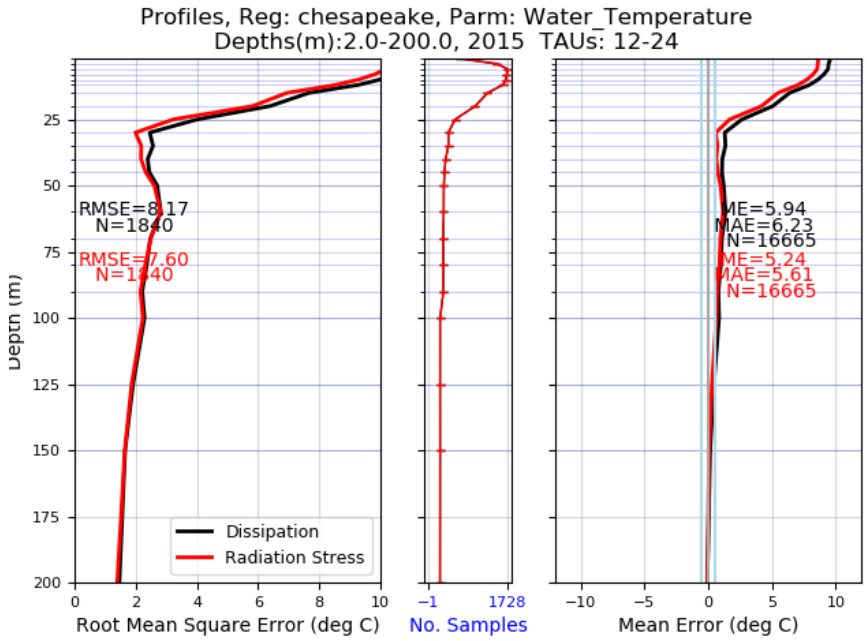

Fig. 33—Temperature Root Mean Square Error (left) and Mean Error (right) for WD (black) and WRSG (red) formulations over the Chesapeake Bay domain.

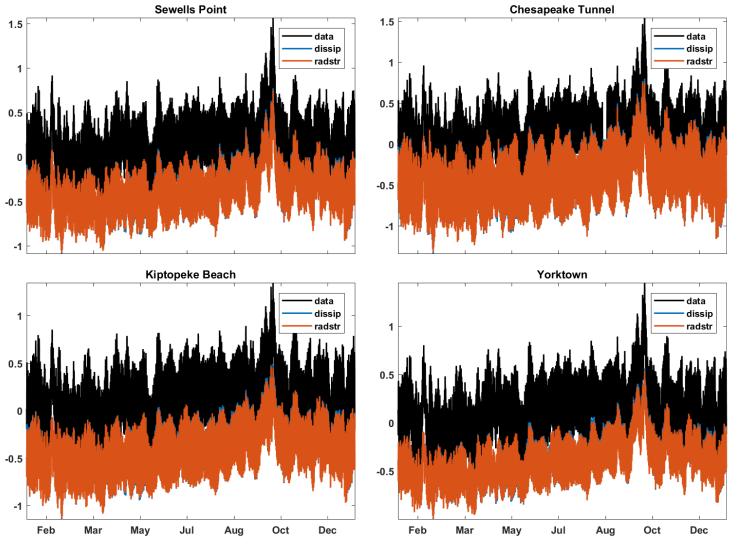

Fig. 34—For Chesapeake Bay domain, water levels (m), observed (black) and modeled using the WD (blue) and WRSG (red) formulations at four water level stations listed in Table 2.

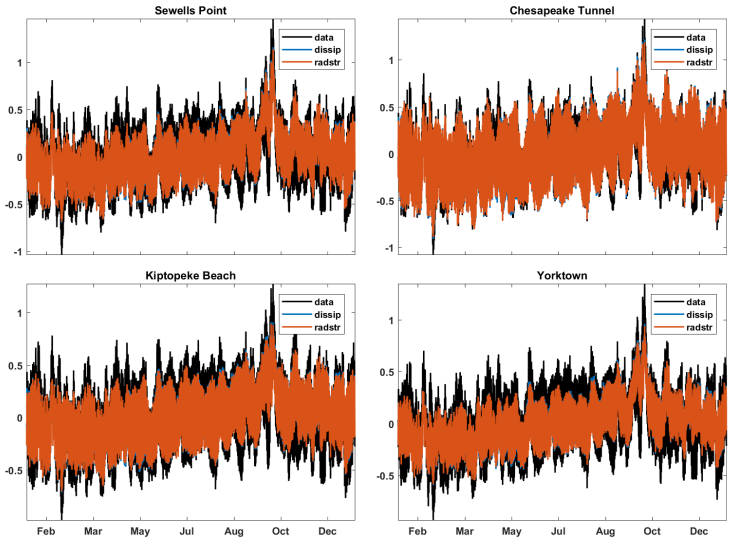

Fig. 35—For Chesapeake Bay domain, water level (m) comparisons, observed (black) and modeled using the WD (blue) and WRSG (red) formulations with biases removed, at four water level stations listed in Table 2.

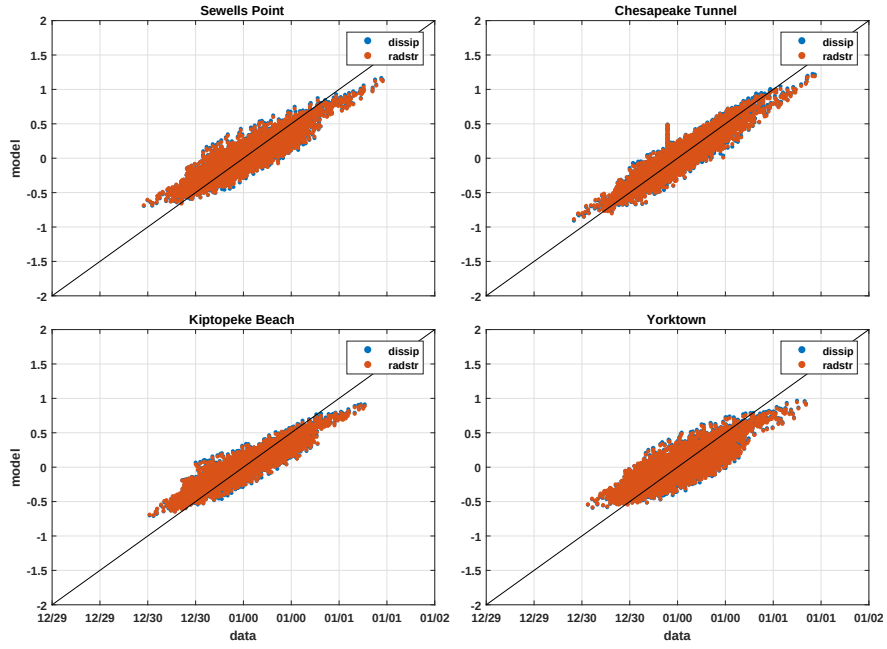

Fig. 36—For Chesapeake Bay domain, water level (m) comparisons over 4 days, for observations (black line) and the WD (blue) and WRSG (red) formulations, at four different tidal stations listed in Table 2.

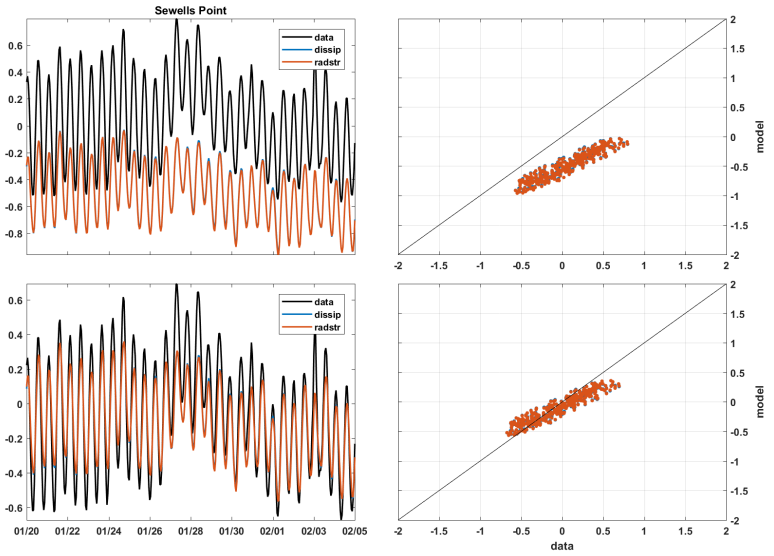

Fig. 37—January Nor'easter water levels (m) at Sewell's Point, observed (black) and modeled using the WD (blue) and WRSG (red) formulations. The bottom panels have the yearly bias from Table 2 removed.

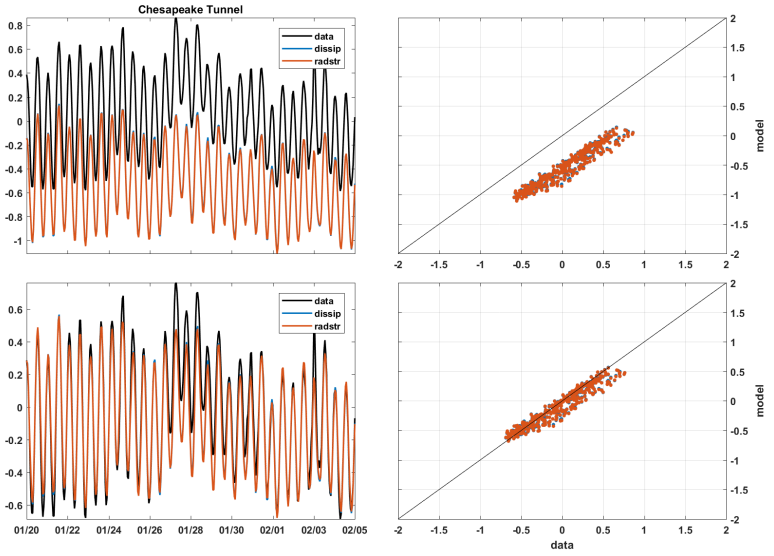

Fig. 38—January Nor'easter water levels (m) at Chesapeake Bay Tunnel, observed (black) and modeled using the WD (blue) and WRSG (red) formulations. The bottom panels have the yearly bias from Table 2 removed.

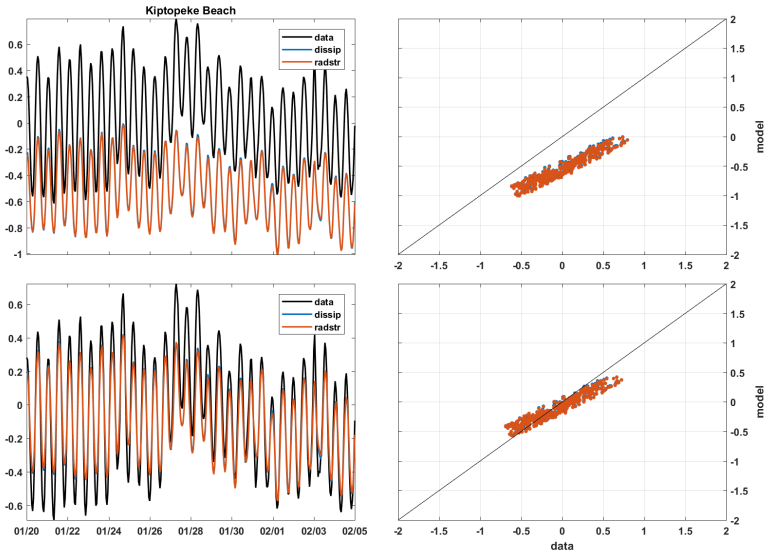

Fig. 39—January Nor'easter water levels (m) at Kiptopeke Beach, observed (black) and modeled using the WD (blue) and WRSG (red) formulations. The bottom panels have the yearly bias from Table 2 removed.

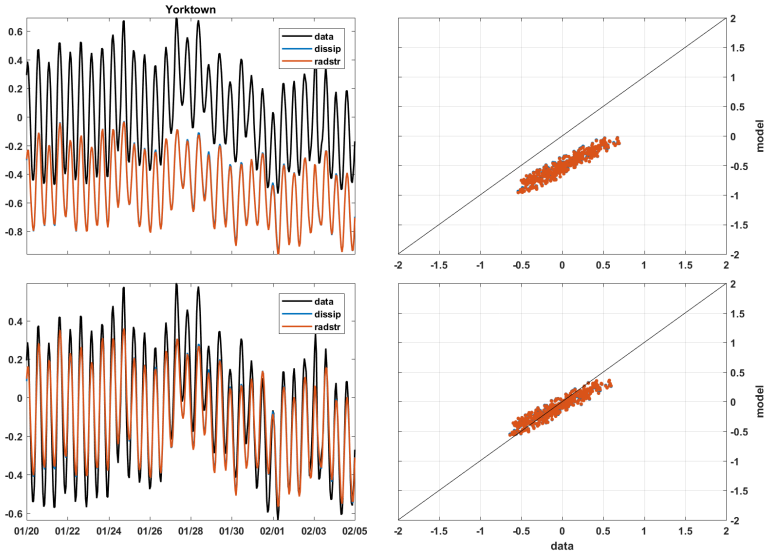

Fig. 40—January Nor'easter water levels (m) at Yorktown, observed (black) and modeled using the WD (blue) and WRSG (red) formulations. The bottom panels have the yearly bias from Table 2 removed.

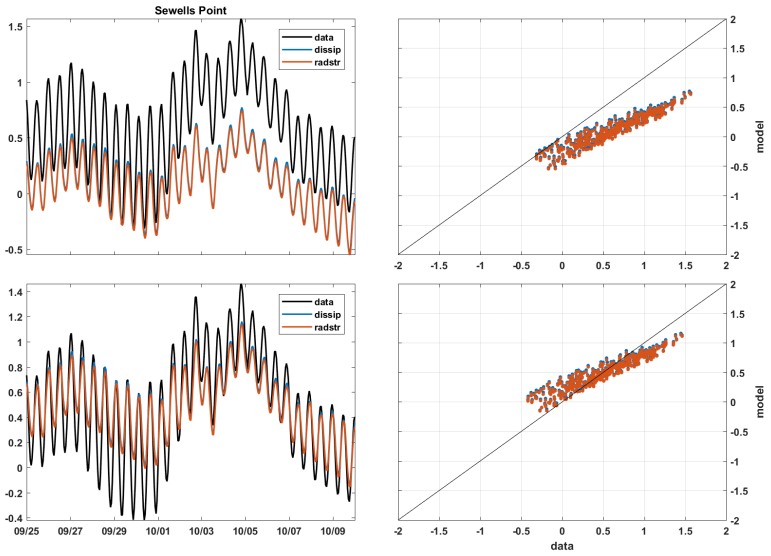

Fig. 41—Hurricane Joaquin water levels (m) at Sewell's Point, observed (black) and modeled using the WD (blue) and WRSG (red) formulations. The bottom panels have the yearly bias from Table 2 removed.

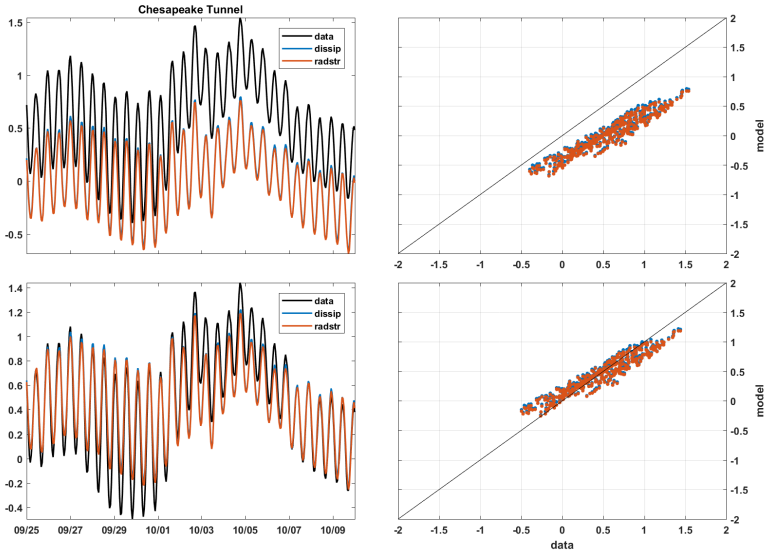

Fig. 42—Hurricane Joaquin water levels (m) at Chesapeake Bay Tunnel, observed (black) and modeled using the WD (blue) and WRSG (red) formulations. The bottom panels have the yearly bias from Table 2 removed.

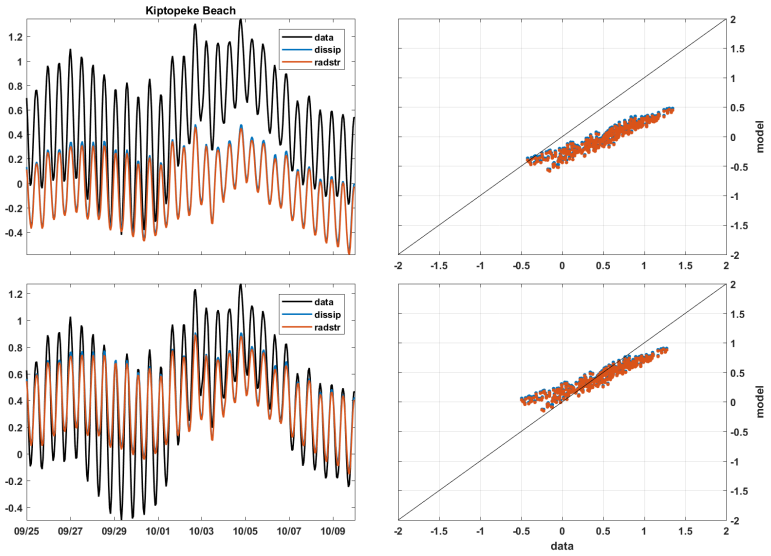

Fig. 43—Hurricane Joaquin water levels (m) at Kiptopeke Beach, observed (black) and modeled using the WD (blue) and WRSG (red) formulations. The bottom panels have the yearly bias from Table 2 removed.

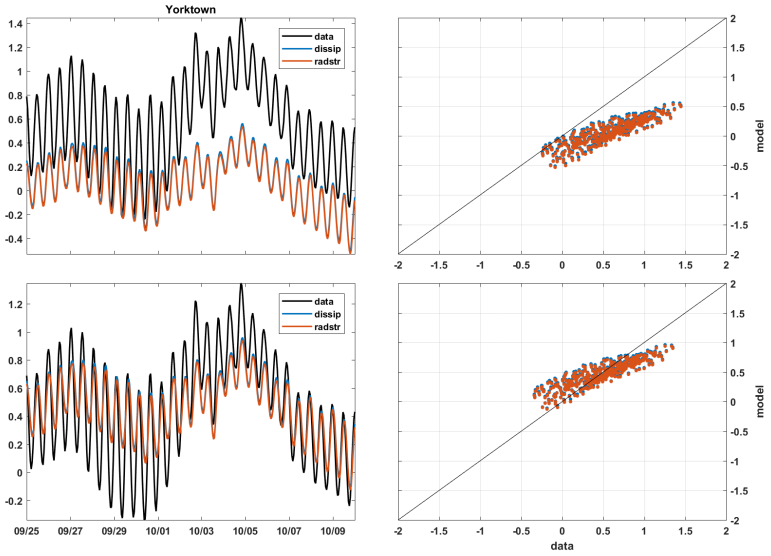

Fig. 44—Hurricane Joaquin water levels (m) at Yorktown, observed (black) and modeled using the WD (blue) and WRSG (red) formulations. The bottom panels have the yearly bias from Table 2 removed.

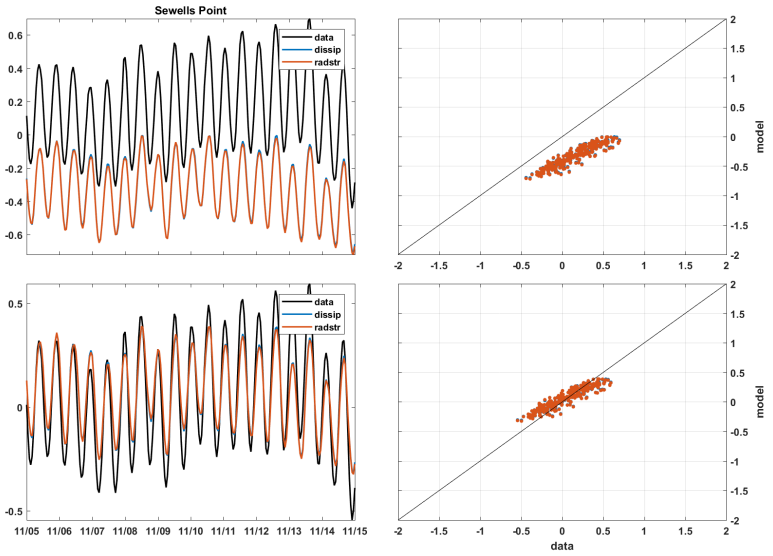

Fig. 45—Hurricane Kate water levels (m) at Sewell's Point, observed (black) and modeled using the WD (blue) and WRSG (red) formulations. The bottom panels have the yearly bias from Table 2 removed.

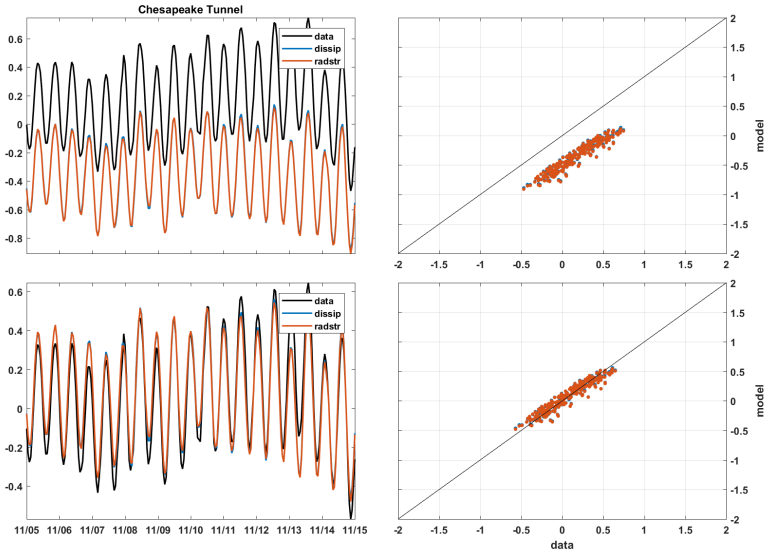

Fig. 46—Hurricane Kate water levels (m) at Chesapeake Bay Tunnel, observed (black) and modeled using the WD (blue) and WRSG (red) formulations. The bottom panels have the yearly bias from Table 2 removed.

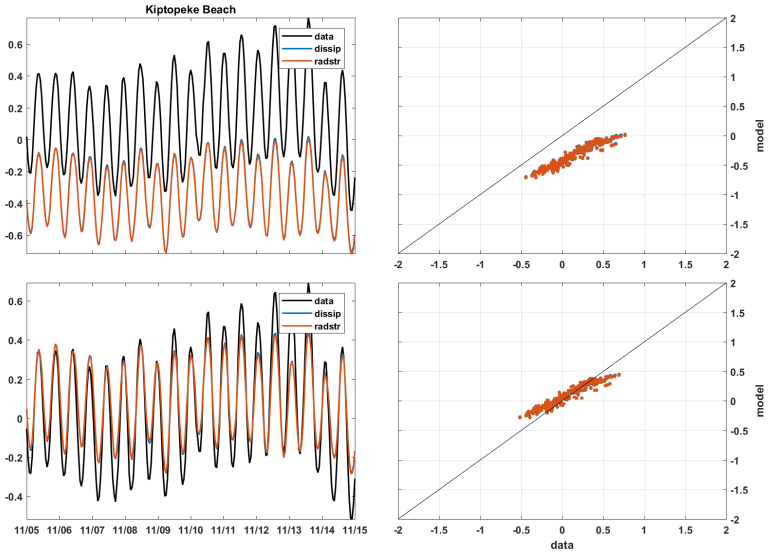

Fig. 47—Hurricane Kate water levels (m) at Kiptopeke Beach, observed (black) and modeled using the WD (blue) and WRSG (red) formulations. The bottom panels have the yearly bias from Table 2 removed.

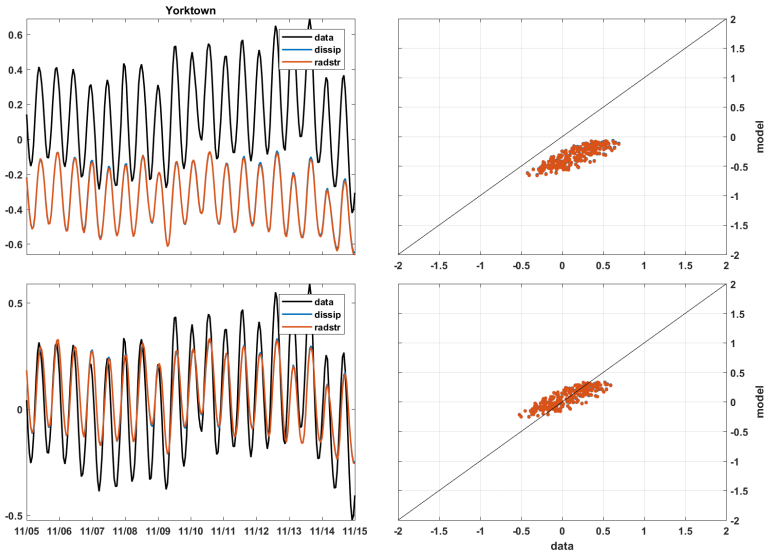

Fig. 48—Hurricane Kate water levels (m) at Yorktown, observed (black) and modeled using the WD (blue) and WRSG (red) formulations. The bottom panels have the yearly bias from Table 2 removed.

5. ACKNOWLEDGEMENTS

This research was accomplished using funding from the Office of Naval Research under the 6.4 program “Small Scale Oceanography” (FY17-PRO-06).

REFERENCES

1. Allard, R. A., T. Smith, T. G. Jensen, P. Y. Chu, E. Rogers, T. Campbell, U. M. Gravois, S. N. Carroll, and K. Watson (2012). "Validation Test Report for the Coupled Ocean/Atmosphere Mesoscale Prediction System (COAMPS) Version 5.0: Ocean/Wave Component Validation," NRL Memorandum Report NRL/MR/7320–12-9423, Naval Research Laboratory, SSC, MS 39529, 91 pp.

2. Allard, R., E. Rogers, P. Martin, T. Jensen, P. Chu, T. Campbell, J. Dykes, T. Smith, J. Choi, and U. Gravois (2014). "The US Navy Coupled Ocean-Wave Prediction System," Oceanography, 27(3), 92–103.

3. Apotsos, A., B. Raubenheimer, S. Elgar, R. T. Guza, and J. A. Smith (2007). "Effects of wave rollers and bottom stress on wave setup," J. Geophys. Res.-Oceans, 112(C2).

4. Avila, L. A. (2016). "Tropical Cyclone Report: Hurricane Kate, 8-11 November 2015," Technical Report AL122015, NOAA, NWS, National Hurricane Center, Miami, FL.

5. Babanin, A. B. and I. R. Young (2005). "Two-phase behavior of the spectral dissipation of wind waves," In: Proc. on Ocean Waves Measurements and Analysis, 5th Int. Symp. on Ocean Waves Measurement and Analyses (WAVES2005), Madrid, Spain, CEDEX, 51.

6. Babanin, A. V., (2006). " On a wave-induced turbulence and a wave-mixed upper ocean layer," Geophys. Res. Lett.,33, L20605.

7. Babanin, A. V. and B. K. Haus (2009). "On the existence of water turbulence induced by nonbreaking surface waves," J. Phys. Oceanogr., 39, 2675–2679.

8. Babanin, A. V., K. N. Tsagareli, I. R. Young, and D. J. Walker (2010). "Numerical Investigation of Spectral Evolution of Wind Waves. Part II: Dissipation Term and Evolution Tests," J. Phys. Oceanogr., 40(4), 667–683.

9. Banner, M. L., A. V. Babanin, and I. R. Young (2000). "Breaking probability for dominant waves on the sea surface," J. Phys. Oceanogr., 30(12), 3145–3160.

10. Barron, C. N., A. B. Kara, P. J. Martin, R. C. Rhodes, and L. F. Smedstad (2006). "Formulation, implementation and examination of vertical coordinate choices in the Global Navy Coastal Ocean Model (NCOM)," Ocean Modelling, 11(3-4), 347–375.

11. Berg, R. (2016). "Tropical Cyclone Report: Hurricane Joaquin, 28 September - 7 October 2015", Technical Report AL112015, NOAA, NWS, National Hurricane Center, Miami, FL.

12. Birkemeier, W. A., C. E. Long, and K. K. Hathaway (1996). "DELILAH, DUCK94 & SandyDuck: Three Nearshore Field Experiments," Coastal Engineering Proceedings, 1(25), 4052–4065.

13. Blumberg, A. F. and G. L. Mellor (1983) "Diagnostic and Prognostic Numerical Circulation Studies of the South-Atlantic Bight," J. of Geophys. Res.-Oceans and Atmos., 88(C8), 4579–4592.

14. Blumberg, A. F. and G. F. Mellor (1987). "A description of a three-dimensional coastal ocean circulation model," In: Heaps, N. S., Ed., Coastal and Estuarine Sciences, Book 4, American Geophysical Union, 1-6, 208 pp.

15. Booij, N., R. C. Ris, and L. H. Holthuijsen (1999). "A third-generation wave model for coastal regions 1. Model description and validation," J. of Geophs. Res.-Oceans, 104(C4), 7649–7666.

16. Campbell, T. J., R. Allard, R. Preller, L. Smedstad, A. Wallcraft, S. Chen, H. Jin, S. Gabersek, R. Hodur, J. Reich, C. D. Fry, V. Eccles, H. P. Cheng, J. R. C. Cheng, R. Hunter, C. DeLuca, and G. Theurich (2010). "Integrated modeling of the battlespace environment," Computing in Science & Engineering, 12(5), 36–45.

17. Charnock, H. (1955). "Wind Stress on a Water Surface," Quart. J. Roy. Meteor. Soc., 81, 639–640.

18. Church, J. C. and E. B. Thorton (1993). "Effects of Breaking Wave-Induced Turbulence within a Longshore Current Model," Coastal Engineering, 20(1-2), 1–28.

19. Craig, P. D. and M. L. Banner (1994). "Modeling Wave-enhanced Turbulence in the Ocean Surface Layer," J. Phys. Oceanogr., 24, 2546–2559.

20. Dingemans, M. W., A. C. Radder, and H. J. Devriend (1987). "Computation of the driving forces of wave-induced currents," Coastal Engineering, 11(5-6), 539–563.

21. Donelan, M. A., A. V. Babanin, I. R. Young, M. L. Banner, and C. McCormick (2005). "Wave-follower field measurements of the wind-input spectral function. Part I: Measurements and calibrations," J. Atmos. and Ocean. Technol., 22(7), 799–813.

22. Donelan, M. A., A. V. Babanin, I. R. Young, and M. L. Banner (2006). "Wave-follower field measurements of the wind-input spectral function. Part II: Parameterization of the wind input," J. Phys. Oceanogr., 36(8), 1672–1689.

23. Grant, W. D. and O. S. Madsen (1979). "Combined Wave and Current Interaction with a Rough Bottom," J. Geophys. Res.-Oceans, 84, 1979–1808.

24. Haas, K. A., and J. C. Warner (2009). "Comparing a quasi-3D to a full 3D nearshore circulation model: SHORECIRC and ROMS," Ocean Modelling, 26, 91–103.

25. Hsu, Y., J. Dykes, R. Allard, and J. Kaihatu (2006). "Evaluation of Delft3D performance in nearshore flows,", Memorandum Report NRL/MR/7320–06-8984, Naval Research Laboratory, Stennis Space Ceneter, MS, 27 pp.

26. Hsu, Y., J. Dykes, R. Allard, and D. Wang (2008). "Validation test report for Delft3d,", 47 pp.

27. Kantha L. H. and C. A. Clayson (2004). "On the Effect of Surface Gravity Waves on Mixing in the Oceanic Mixed Layer," Ocean Modelling 6, 101–124.

28. Kumar, N., G. Voulgaris, and J. C. Warner (2011). "Implementation and modification of a three-dimensional radiation stress formulation for surf-zone and rip-current applications", Coastal Engineering, 58(12), 1097–1117.

29. Kumar, N., G. Voulgaris, J. C. Warner, and M. Olabarrieta (2012). "Implementation of the vortex force formalism in the coupled ocean-atmosphere-wave-sediment transport (COAWST) modeling system for inner shelf and surf zone applications," Ocean Modelling, 47, 65–95.

30. Lippmann, T. C., A. H. Brookins, and E. B. Thornton (1996). "Wave energy transformation on natural profiles," Coastal Engineering, 27(1-2), 1–20.

31. Longuet-Higgins, M.S. and R.W. Stewart (1962). "Radiation stress and mass transport in gravity waves, with application to surf beats," Journal of Fluid Mechanics, 13(4), 481–504.

32. Longuet-Higgins, M.S., and R.W. Stewart (1964). "Radiation stresses in water waves: a physical discussion with applications," Deep-Sea Res., 11, 529–562.

33. Martin, P. J., E. Rogers, R. A. Allard, J. D. Dykes, and P. J. Hogan (2013). "Tests of Parameterized Langmuir-Circulation Mixing in the Ocean's Surface Mixed Layer," NRL Memorandum Report NRL/MR/7320–13-9444, Naval Research Laboratory, SSC, MS 39529, 47 pp.

34. Martin, P. J., G. Peggion, and K. J. Yip (1998). "A comparison of several coastal ocean models," Technical Report NRL/FR/7322–97–9692, Naval Research Laboratory, Stennis Space Center, MS.

35. McWilliams, J. C., J. M. Restrepo, and E. M. Lane, (2004). "An asymptotic theory for the interaction of waves and currents in coastal waters," Journal of Fluid Mechanics, 511, 35–178.

36. Mellor, G. L. (2002). "Oscillatory Bottom Boundary Layers," J. Phys. Oceanogr., 32, 3075–3088.

37. Mellor, G. L. (2003). "The Three-Dimensional Current and Surface Wave Equations," J. Phys. Oceanogr., 33, 1978–1989.

38. Mellor, G. L. (2005). "Some Consequences of the Three-Dimensional Current and Surface Wave Equations," J. Phys. Oceanogr., 35, 2291–2298.

39. Mellor, G. L. (2008). "The Depth-Dependent Current and Wave Interaction Equations: A Revision," J. Phys. Oceanogr., 38, 2587–2596.

40. Mellor, G. L. (2011). "Wave radiation stress," Ocn. Dyn., 61, 563–568.

41. Mellor, G. L. (2013). "Waves, circulation and vertical dependence," Ocn. Dyn., 63, 447–457.

42. Mellor, G. L. (2015). "A Combined Derivation of the Integrated and Vertically Resolved, Coupled Wave–Current Equations," J. Phys. Oceanogr., 45, 1453–1463.

43. Mellor, G. L. (2016). "On theories dealing with the interaction of surface waves and ocean circulation," J. Geophys. Res.-Oceans, 121(7), 4474–4486.

44. Mellor, G. L. (2017). Reply to "Comments on 'A Combined Derivation of the Integrated and Vertically Resolved, Coupled Wave–Current Equations'," J. Phys. Oceanogr., 47, 2387–2389.

45. Nairn, R. B., J. A. Roelvink, and H. N. Southgate (1990). "Transition zone width and impliations for modeling surf zone hydrodynamics," In: Proceedings of the 22nd International Conference on Coastal Engineering, American Society of Civil Engineers, 68–81.

46. Reniers, A. J. H. M and J. A. Battjes (1997). "A laboratory study of longshore currents over barred and non-barred beaches," Coastal Engineering, 30(1-2), 1–21.

47. Reniers, A. J. H. M., E. B. Thornton, and T. C. Lippmann (1995). "Longshore currents over barred beaches," In: Coastal Dynamics '95: Proceedings of the International Conference on Coastal Research in Terms of Large Scale Experiments : Gdansk, Poland September 4-8, 1995, by International Conference on Coastal Research in Terms of Large Scale Experiments, Gdansk, Poland, Sep. 04-08, with editors W. R. Dally and R. B. Zeidler, Amer. Soc. Civil Engineers, New York 413–424.

48. Roelvink, J. A. and M. J. F. Stive, (1989). "Bar-generating Cross-shore Flow Mechanisms on a Beach," J. Geophys. Res.-Oceans, 94(C4), 4785–4800.

49. Rogers, W. E., A. V. Babanin, and D. W. Wang (2012). "Observation-Consistent Input and Whitecapping Dissipation in a Model for Wind-Generated Surface Waves: Description and Simple Calculations," J. of Atmos. Ocean. Technol., 29(9), 1329–1346.

50. Ruessink, B. G., J. R. Miles, F. Feddersen, R. T. Guza, and S. Elgar (2001). "Modeling the alongshore current on barred beaches," J. Geophys. Res.-Oceans, 106(C10), 22451–22463.

51. Smith, J. M., M. Larson, and N. C. Kraus (1993). "Longshore-current in a Barred Beach - Field-Measurements and Calculation," J. of Geophys. Res.-Oceans, 98(C12), 22717–22731.

52. Soulsby, R.L. (1995). "Bed Shear-Stresses Due to Combined Waves and Currents," In: Advances in Coastal Morphodynamics, edited by M. Stive, J. Fredsoe, L. Hamm, R. Soulsby, C. Teisson, and J. Winterwerp, Delft Hydraulics, Delft, The Netherlands, 420–423.

53. Svendsen, I. A. (1984a) "Wave Heights and Setup in a Surf Zone," Coastal Engineering, 8(4),303–329.

54. Svendsen, I. A. (1984b). "Mass Flux and Undertow in a Surf Zone," Coastal Engineering, 8(4), 347–365.

55. Tang, C. L., W. Perrie, A. D. Jenkins, B. M. DeTracey, Y. Hu, B. Toulany, and P. C. Smith (2007). "Observation and modeling of surface currents on the Grand Banks: A study of the wave effects on surface currents," Journal of Geophys. Res.-Oceans, 112.

56. Tsagareli, K. N., A. V. Babanin, D. J. Walker, and I. R. Young (2010). "Numerical Investigation of Spectral Evolution of Wind Waves. Part I: Wind-Input Source Function." J. Phys. Oceanogr., 40(4), 656–666.

57. Uchiyama, Y., J. C. McWilliams, and A. F. Shchepetkin (2010). "Wave-current interaction in an oceanic circulation model with a vortex-force formalism: Application to the surf zone", Ocean Modelling, 34, 16–35.

58. Warner, J. C., C. R. Sherwood, R. P. Signell, C. K. Harris, and H. G. Arango (2008). "Development of a three-dimensional, regional, coupled wave, current, and sediment-transport model," Computers & Geosciences, 34(10), 1284–1306.

59. Young, I. R. and A. V. Babanin (2006). "Spectral distribution of energy dissipation of wind-generated waves due to dominant wave breaking," J. Phys. Oceanogr., 36(3), 376–394.